

UNCLASSIFIED

AD NUMBER

AD805556

LIMITATION CHANGES

TO:

Approved for public release; distribution is unlimited.

FROM:

Distribution authorized to U.S. Gov't. agencies and their contractors;  
Administrative/Operational Use; DEC 1966. Other requests shall be referred to Ballistic Systems Div., Norton AFB, CA.

AUTHORITY

SAMSO ltr 28 Feb 1972

THIS PAGE IS UNCLASSIFIED

805556

**THE PRODUCTION OF NITRIC OXIDE  
IN SHOCK-HEATED AIR**

**Morton Camas, Robert M. Feinberg, and J. Derek Teare**

**RESEARCH REPORT 245**

**December 1966**

**supported jointly by**

**BALLISTIC SYSTEMS DIVISION  
DEPUTY FOR BALLISTIC MISSILE RE-ENTRY SYSTEMS  
AIR FORCE SYSTEMS COMMAND  
Horton Air Force Base, California  
under Contract No. AF 04(694)-690**

**ADVANCED RESEARCH PROJECTS AGENCY**

**monitored by the  
ARMY MISSILE COMMAND  
UNITED STATES ARMY  
Redstone Arsenal, Alabama  
under Contract No. DA-01-021-AMC-12005 (Z)  
(part of Project DEFENDER)**



**EVERETT RESEARCH LABORATORY**

**A DIVISION OF AVCO CORPORATION**

**D D C  
RECEIVED  
JAN 27 1967  
A**

**BEST  
AVAILABLE COPY**

THE PRODUCTION OF NITRIC OXIDE IN SHOCK-HEATED AIR

by

Morton Camac, Robert M. Feinberg and J. Derek Teare

AVCO EVERETT RESEARCH LABORATORY  
a division of  
AVCO CORPORATION  
Everett, Massachusetts

December 1966

supported jointly by

BALLISTIC SYSTEMS DIVISION  
DEPUTY FOR BALLISTIC MISSILE RE-ENTRY SYSTEMS  
AIR FORCE SYSTEMS COMMAND  
Norton Air Force Base, California

under Contract No. AF 04(694)-690

ADVANCED RESEARCH PROJECTS AGENCY  
monitored by the  
ARMY MISSILE COMMAND  
UNITED STATES ARMY  
Redstone Arsenal, Alabama  
under Contract No. DA-01-021-AMC-12005(Z)  
(part of Project DEFENDER)

THIS DOCUMENT IS SUBJECT TO SPECIAL  
EXPORT CONTROLS AND EACH TRANS-  
MITTAL TO FOREIGN GOVERNMENTS OR  
FOREIGN NATIONALS MAY BE MADE  
ONLY WITH PRIOR APPROVAL OF:  
BALLISTIC SYSTEMS DIVISION (B8YDV)  
NORTON AFB, CALIF. 92408.

## FOREWORD

This report has been supported jointly by Avco Everett Research Laboratory under Contract No. AF 04(694)-690 for Ballistic Systems Division, Deputy for Ballistic Missile Re-entry Systems, Air Force Systems Command, Norton Air Force Base, California, and Advanced Research Projects Agency monitored by the Army Missile Command, United States Army, Redstone Arsenal, Alabama under Contract No. DA-01-021-AMC-12005(Z) (part of Project DEFENDER). The secondary report number as assigned by AERL is Avco Everett Research Report 245. The Air Force program monitor for Contract AF 04(694)-690 is Thomas W. Swartz, 1st Lt., USAF Project Officer.

Publication of this report does not constitute Air Force approval of the report's findings or conclusions. It is published only for the exchange and stimulation of ideas.

Thomas W. Swartz, 1st Lt.  
USAF, Project Officer

## ABSTRACT

The rate of production of nitric oxide in shock-heated air was measured over the temperature range from 2300°K to 4500°K. The NO concentration was determined from the NO infrared emission in the 5.3 micron fundamental vibration-rotation band. The main production of nitric oxide was found to be by the dissociation reaction  $O_2 + M \xrightarrow{k_4} 2O + M$ , followed by the atomic shuttle reactions  $O + N_2 \xrightarrow{k_2} NO + N$  and  $N + O_2 \rightarrow NO + O$ . The overall rate constant  $k = k_2 \cdot k_4$  for NO production was found to be  $0.40 \pm 0.12$  of the rate constant compiled by Wray.

The rate constant for the bimolecular reaction  $N_2 + O_2 \rightarrow 2NO$  was found to be less than one-tenth the value suggested by Freedman and Daiber. In order to explain the disagreement in the rate constant, experiments were performed in shock-heated nitric oxide where the depletion of nitric oxide and the reaction products were observed. It was found that the NO depletion occurs mainly via the reaction  $2NO \rightarrow N_2O + O$ .

An analysis of the vibrational relaxation of NO-O<sub>2</sub>-N<sub>2</sub> mixtures is presented and it is shown that NO vibration lag is small and does not affect the data analysis. We determined that the integrated band intensity of the NO fundamental is  $124 \pm 22 \text{ atm}^{-1} \text{ cm}^{-2}$  at S. T. P.

It is also shown that corrections due to the shock tube boundary layer must be included in order to obtain detailed agreement between experiment and calculations. The procedure for correcting chemical measurements for shock tube boundary layer growth is outlined.

## TABLE OF CONTENTS

	<u>Page</u>
Foreword	ii
Abstract	iii
I. INTRODUCTION	1
II. THEORY OF EXPERIMENT	3
III. EXPERIMENTAL MEASUREMENTS	7
IV. DISCUSSION OF RESULTS	15
Appendix A - NO VIBRATION RELAXATION IN AIR	26
Appendix B - CALIBRATION OF INFRARED SYSTEM	32
Appendix C - EFFECTS OF BOUNDARY LAYER GROWTH ON SHOCK TUBE WALLS	39
References	45

## I. INTRODUCTION

Interest in the chemical reaction rates in high temperature air arises in many combustion studies, such as in controlled flame reactions and in rocket motors. Also, chemical changes in shocked air become significant in high speed flight above Mach 6. Nitric oxide (in equilibrium) is an important constituent of air above 2000°K.<sup>1</sup> Several authors<sup>2-4</sup> have tabulated the various reaction paths for the production of NO starting with N<sub>2</sub>-O<sub>2</sub> mixtures. For many of these reactions, the rate constants were measured over a small temperature interval, and theoretically extrapolated over a wide temperature range. The purpose of this work was to determine the rate of production of NO in shock heated air. This is an integral type experiment in that many reactions take place simultaneously. Our results were then compared to calculated NO production rates in air based on the reaction rate constants compiled by Wray.<sup>4</sup>

An extensive high temperature shock tube study of NO formation in N<sub>2</sub>-O<sub>2</sub> mixtures, diluted in Ar, was performed by Glick, Klein and Squire<sup>5</sup> employing the single pulse shock tube method. The gas resided at a high temperature for several milliseconds, and then cooled quickly. Then a gas sample was taken from the shock tube and analyzed for NO. The argon acted as an additional catalyst for quickly bringing the atomic oxygen concentration to equilibrium.<sup>6</sup> Thus, they were able to determine the rate constants for the NO producing reaction,  $O + N_2 \rightarrow NO + N$ . This reaction, followed by the faster reaction  $N + O_2 \rightarrow NO + O$ , forms a pair of NO producing reactions with the atoms acting as catalysts. In the case of air, the atomic oxygen is produced either by  $O_2 + M \rightarrow 2O + M$  (where  $M = N_2$  or  $O_2$ )<sup>7,8</sup> or  $N_2 + O_2 \rightarrow N_2O + O$ . The rate constant for the latter reaction has not been determined and its importance for temperatures above 2000°K is not known. Before these atom reactions become important, the initial production of NO is reported to be by the reaction  $N_2 + O_2 \rightarrow 2NO$ ;<sup>9-11</sup> however, in the present experiment this reaction is negligible. Our measurements of the rate of



NO formation in shock heated air were compared to calculations based on the rate constants for the above reactions.

In addition to the single pulsed shock tube method<sup>5</sup> discussed above, several other methods for determining NO in shock heated air exist. The ultraviolet absorption<sup>9,11</sup> and the NO infrared emission in the vibration-rotation band<sup>12,13</sup> techniques have been employed for observing the NO vibrational relaxation and decomposition rates. At lower temperatures, NO reactions have been studied in flames<sup>14</sup> and flow tubes.<sup>10</sup> In this paper, the NO infrared emission technique was employed.

The theory of the experiment is discussed in the next section. The experimental measurements of the NO infrared emission from shock heated air follows. In the final section, our measurements are compared to NO production calculations. The important conclusions are summarized.

There are three appendices in this report. In the first, the theory of vibrational relaxation in a mixture of diatomic molecules is reviewed. Numerical results are presented for the vibrational relaxation of a trace amount of NO in air over the temperature range from 2000°K to 6500°K. In the second appendix, band intensity formulation is developed and applied to the calibration of the infrared system. These formulas were used in Section III to determine the NO fundamental band strength. It is also shown that the weak line approximation is valid for our shock tube data. In the final appendix, the procedure for correcting the chemical measurements for the effects of shock tube boundary layer growth is developed and then applied to the NO formation chemistry.

## II. THEORY OF EXPERIMENT

The main purpose of this paper is to determine the rate of formation of NO in shock heated air. The NO concentration was determined from the NO infrared emission in the 5.3 micron fundamental vibration rotation band. In order to evaluate the experimental data, the gas conditions downstream of the shock and the sensitivity of the infrared system to the NO concentration and vibrational temperature were determined.

Experimental data have been obtained over the shock velocity range from 2.0 to 4.5 mm per microsecond, and at initial air pressures from 1 to 50 torr. The shock heated gas temperature and density are shown in Figs. 1 and 2 for three chemical states of air -- frozen vibration, equilibrium vibration and frozen chemistry, and full chemical equilibrium. The equilibrium species concentrations are presented as a function of incident shock velocity in Fig. 3. These conditions were computed by combining the Rankine-Hugoniot shock relations with the equation of state for air. The calculations of thermodynamic properties and composition of equilibrium air were based on published spectroscopic data.<sup>15,16</sup> Note that in equilibrium, oxygen dissociation becomes appreciable and the NO concentration reaches several percent. The heavy lines in Figs. 1 and 2 indicate the range of experimental data.

The intensity of the radiation from the entire 5.3 micron band is directly related to the vibrational energy even for nonequilibrium vibrational distributions. This can be shown as follows: the energy  $E$  invested in vibration is

$$E = \sum_m N_m E_m \quad (1)$$

$N_m$  and  $E_m$  are the number density and energy of the  $m^{\text{th}}$  vibrational level. In the harmonic oscillator approximation, this becomes

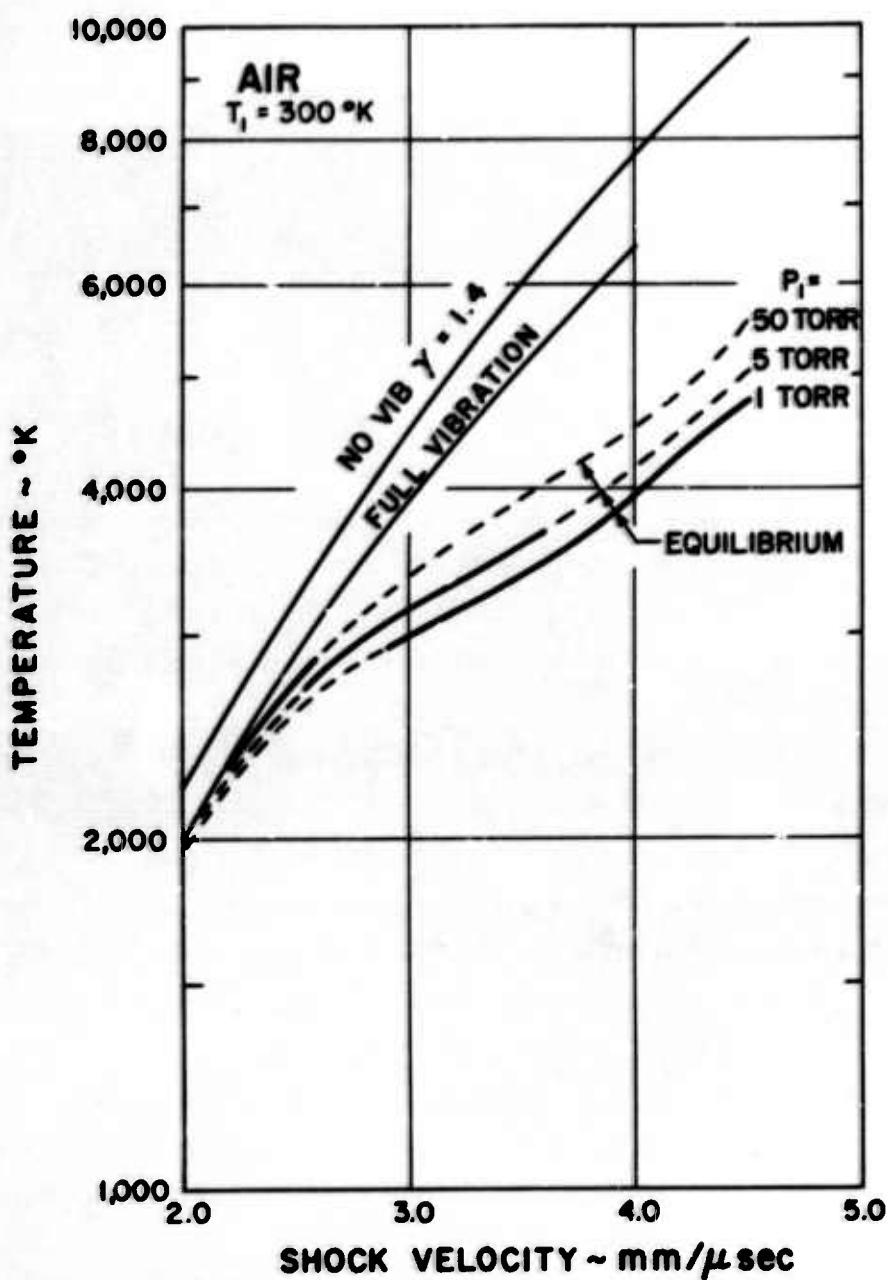


Fig. 1 Temperature of shock heated air as a function of shock velocity for several initial pressures. The heavy lines indicate the range of the experimental data.

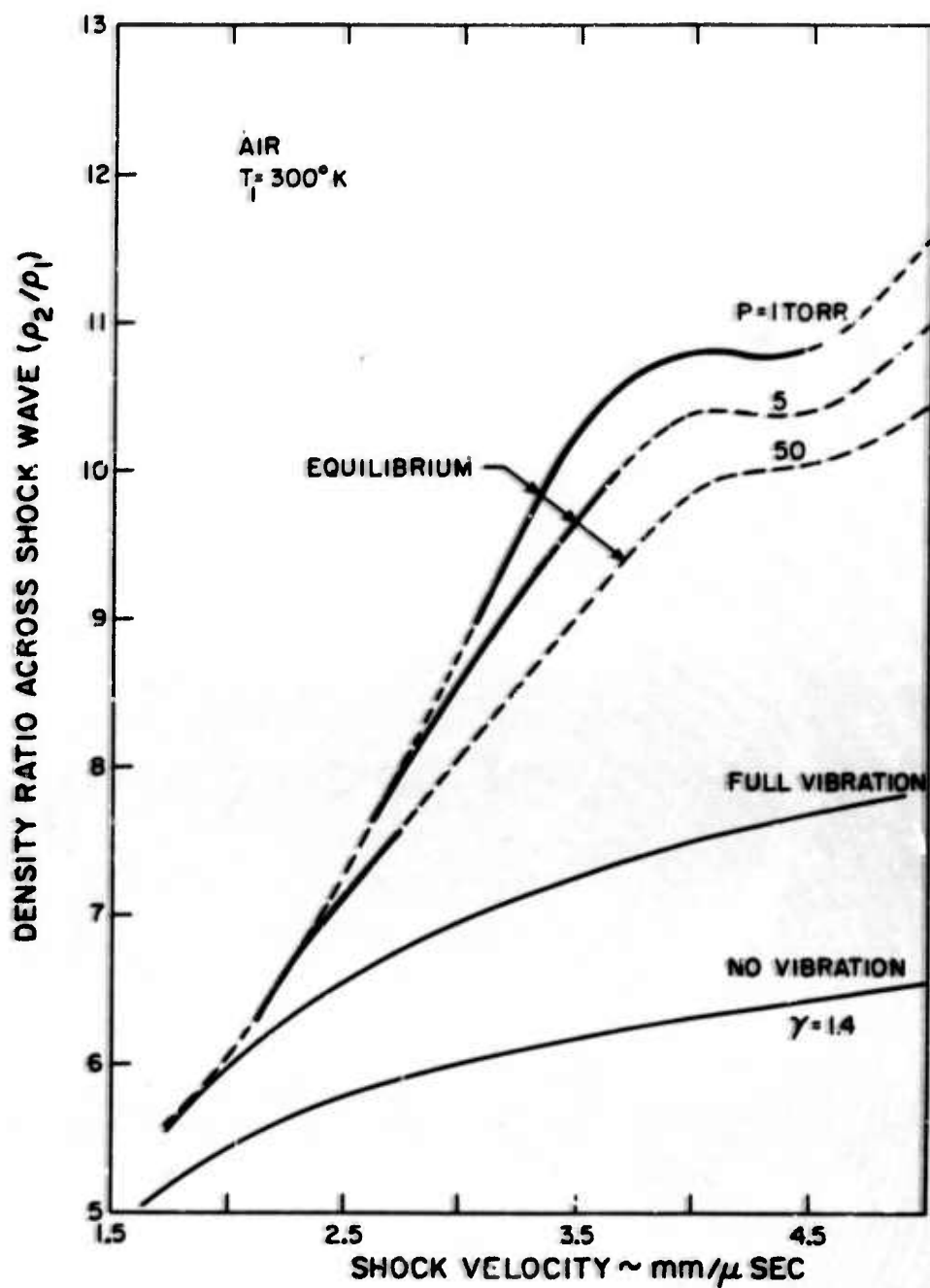


Fig. 2 Density of shock heated air as a function of shock velocity for several initial pressures. The heavy lines indicate the range of the experimental data.

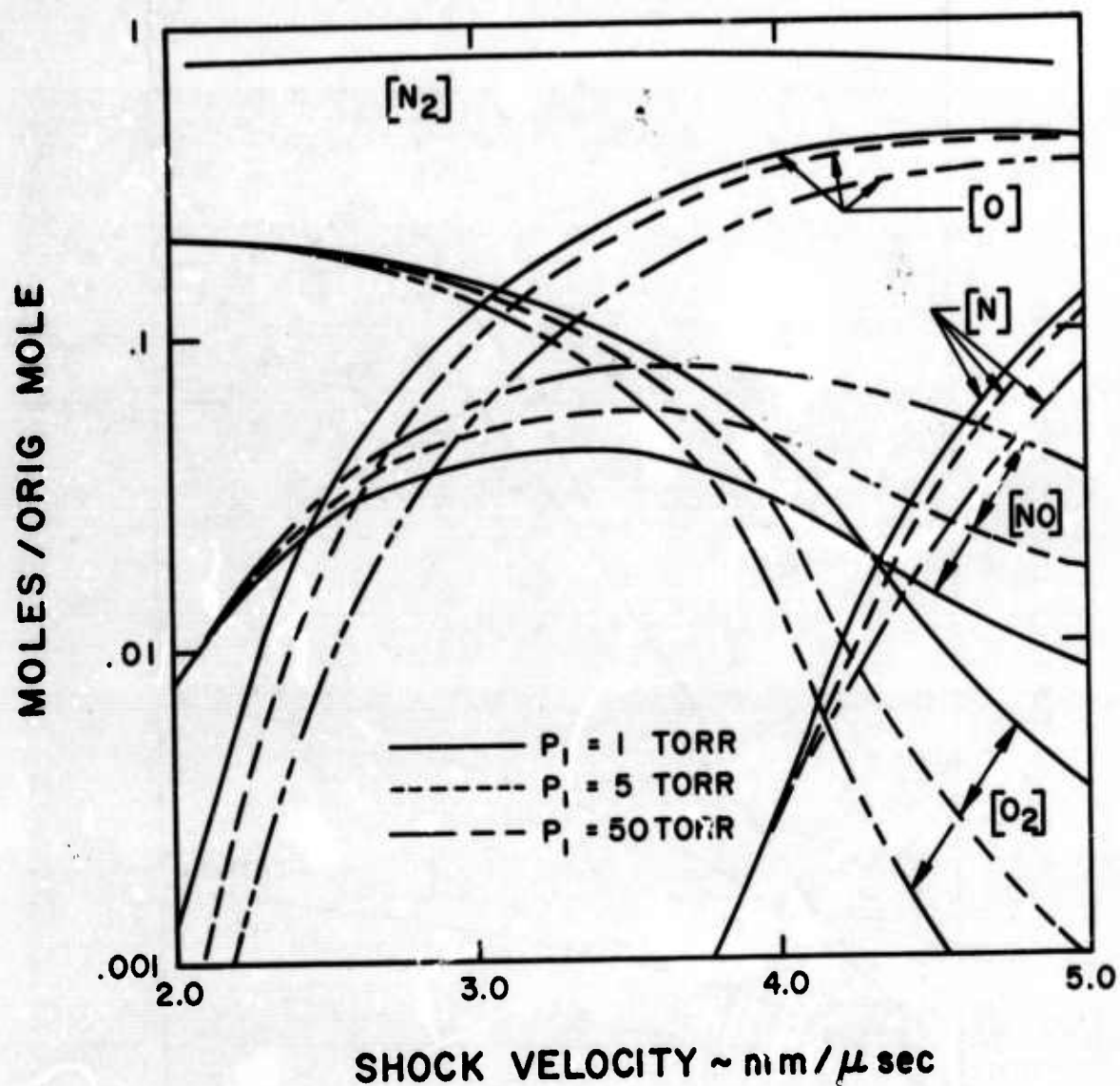


Fig. 3 Species concentrations at chemical equilibrium as a function of shock velocity for several initial pressures.

$$E = \sum_m N_m m E_0 \quad (2)$$

where  $E_0$  is the energy gap between equally spaced levels. In the same approximation, the infrared emission,  $I$ , is due to the radiative transitions between adjacent levels.

$$I = \sum_m \frac{N_m (h\nu_m)}{\tau_m} \quad (3)$$

where  $h\nu_m = E_0$  and  $\tau_m$  are the photon energy and the lifetime of the  $m^{\text{th}}$  level. The lifetime,  $\tau_m$ , determined from the dipole selection rule for harmonic oscillators, is  $\tau_m = \tau_1/m$ . (In this paper, we find that  $\tau_1$  is approximately 0.1 second for the NO fundamental.) Substituting for  $h\nu_m$  and  $\tau_m$  in Eq. (3), and noting the similarity with Eq., (2),

$$I = \frac{1}{\tau_1} \sum_m N_m m E_0 = \frac{E}{\tau_1} \quad (4)$$

Thus, in the harmonic oscillator approximation, the infrared emission is directly proportional to the vibrational energy. In practice, the coupling between vibrational and rotational modes must be included; however, the emission from the entire band remains within a few percent of that given by Eq. (4).

#### NO Vibrational Relaxation in Air

In the harmonic oscillator approximation, the vibrational energy is related to the vibrational temperature,  $T_v$ , by the relation

$$E = \frac{NE_0}{e^{E_0/kT_v} - 1} \quad (5)$$

where  $N$  is the number density of NO molecules and  $k$  is the Boltzmann constant. It has been shown<sup>17</sup> that, in an abrupt change in the gas temperature causing vibrational lag, the vibrational level population adjusts so



that a vibrational temperature  $T_v$  exists during the relaxation process.

In order to relate the infrared emission,  $I$ , to the NO concentration,  $N$ , by Eq. (5), the NO vibrational temperature must be known. In a chemical experiment, the infrared signal can be used as a direct measure of the NO concentration only when the NO vibrational and translational temperatures are equal. However, immediately behind the shock, the vibrational temperature of NO (also of  $N_2$  and  $O_2$ ) is less than the kinetic temperature, and the infrared emission is less than that for equilibrium. Thus, a correct interpretation of the infrared signal requires a knowledge of the vibrational relaxation rates. The general problem of vibrational coupling between NO,  $O_2$  and  $N_2$  is considered in detail in Appendix A. The results of these calculations are reviewed in Section IV where they are applied to the experimental data. Fortunately, the vibrational lag correction to the data is small.

#### Chemical Reactions for NO Formation

The chemical reactions leading to NO production have been reviewed in the literature.<sup>2-4</sup> While over a score of possible reactions are tabulated, there are only a few important reactions and these can be arranged in three groups:

- (1) Direct production of NO by the reaction

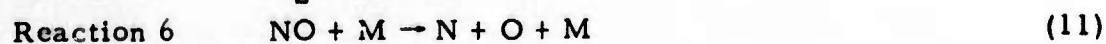


- (2) Atomic shuttle reactions which convert  $N_2$  and  $O_2$  to 2NO



These reactions have an incubation time until there is sufficient production of atomic oxygen; at such time they become the dominant reactions producing NO.

- (3) Atom producing reactions



M can be any of the atoms or molecules shown in Reactions 1 to 6.

The reaction  $N_2 + O_2 \rightarrow N_2O + O$  could also be a source of atomic oxygen, but its rate is not known.

Our experimental measurements were compared to calculated NO formation rates which were based on the rate constants compiled by Wray<sup>4</sup> and shown in Table I. These rates were varied in order to determine the NO production sensitivity to the rate constants. A comparison of these calculations with the data is presented in Section IV.



TABLE 1 RATE CONSTANTS FOR CHEMICAL PROCESSES<sup>4</sup>

#	REACTION	CATALYST M	RATE CONSTANT EXPRESSION
(1)	$N_2 + O_2 + 1.9 \text{ ev} \rightleftharpoons 2NO$	----	$k_1 = 9.1 \times 10^{24} T^{-5/2} \exp(-128,500/RT)$
(2)	$N_2 + O + 3.3 \text{ ev} \rightleftharpoons NO + N$	----	$k_2 = 7 \times 10^{13} \exp(-75,500/RT)$
(3)	$O_2 + N \rightleftharpoons NO + O + 1.4 \text{ ev}$	----	$k_3 = 1.34 \times 10^{10} T \exp(-43,500/RT)$
(4)	$O_2 + M + 5.1 \text{ ev} \rightleftharpoons 2O + M$ D = 118,000	Ar, N, NO  N <sub>2</sub>  O <sub>2</sub>  O	$k_4 = 2.5 \times 10^{11} T^{1/2} (D/RT)^{3/2} \exp(-D/RT)$  2k <sub>4</sub> , Ar  9k <sub>4</sub> , Ar  25k <sub>4</sub> , Ar
(5)	$N_2 + M + 9.8 \text{ ev} \rightleftharpoons 2N + M$ D = 224,900	Ar, O, O <sub>2</sub> , NO  N <sub>2</sub>  N	$k_5 = 1.7 \times 10^{12} T^{1/2} (D/RT) \exp(-D/RT)$  4.2 × 10 <sup>12</sup> T <sup>1/2</sup> (D/RT) exp(-D/RT)  3.2 × 10 <sup>12</sup> T <sup>1/2</sup> (D/RT) <sup>2</sup> exp(-D/RT)
(6)	$NO + M + 6.5 \text{ ev} \rightleftharpoons N + O + M$ D = 150,000	Ar, O <sub>2</sub> , N <sub>2</sub> NO, O, N	$k_6 = 7.0 \times 10^{10} T^{1/2} (D/RT)^2 \exp(-D/RT)$  20k <sub>6</sub> , Ar

### III. EXPERIMENTAL MEASUREMENTS

#### Experimental Apparatus

The experiments were carried out in a 1.5 inch diameter stainless steel shock tube composed of a driver, a 22 foot long low pressure section, and a large expansion tank at the upstream end. X-scribed stainless steel diaphragms were ruptured by high pressure  $H_2$  or  $H_2-N_2$  mixtures. A 10 mil cellophane diaphragm separated the low pressure section from the expansion tank. To maintain a low impurity level and also to reduce the pumping time, special valves were developed which permitted changing diaphragms at the driver and expansion tank while the shock tube was under a partial vacuum. Thus, room air did not enter the shock tube between runs. These valves had an auxiliary chamber in which new diaphragms could be pumped on and out-gassed before insertion in the shock tube. The shock tube was evacuated to a pressure of  $2 \times 10^{-5}$  torr or lower by an oil diffusion pump with a liquid  $N_2$  cooled trap. The leak rate after sealing off the shock tube was approximately 0.3 microns Hg per minute. Since the initial gas was dried room air, the effects of this small air leak on the chemistry was negligible.

The shock velocity was measured with a series of platinum resistance heat transfer gauges spaced several feet apart. The heat transfer signals were displayed on a raster oscilloscope. The distance between gauges was measured to  $\pm 0.01$  inch and the time between stations was determined to  $1/2$  microsecond. The maximum error in the shock velocity determination was  $\pm 0.65\%$ . The shock velocity attenuation was constant along the length of the tube and was only a function of shock velocity: 0.20 mm per microsecond per meter length of tube at the high velocities, and 0.074 mm per microsecond per meter length of the tube at the low velocities. Where the effects of shock attenuation became important, the data were not analyzed in detail.

A schematic diagram of the section of the shock tube for the infrared measurements is shown in Fig. 4. This section, located 18 feet from the

## EXPERIMENTAL ARRANGEMENT

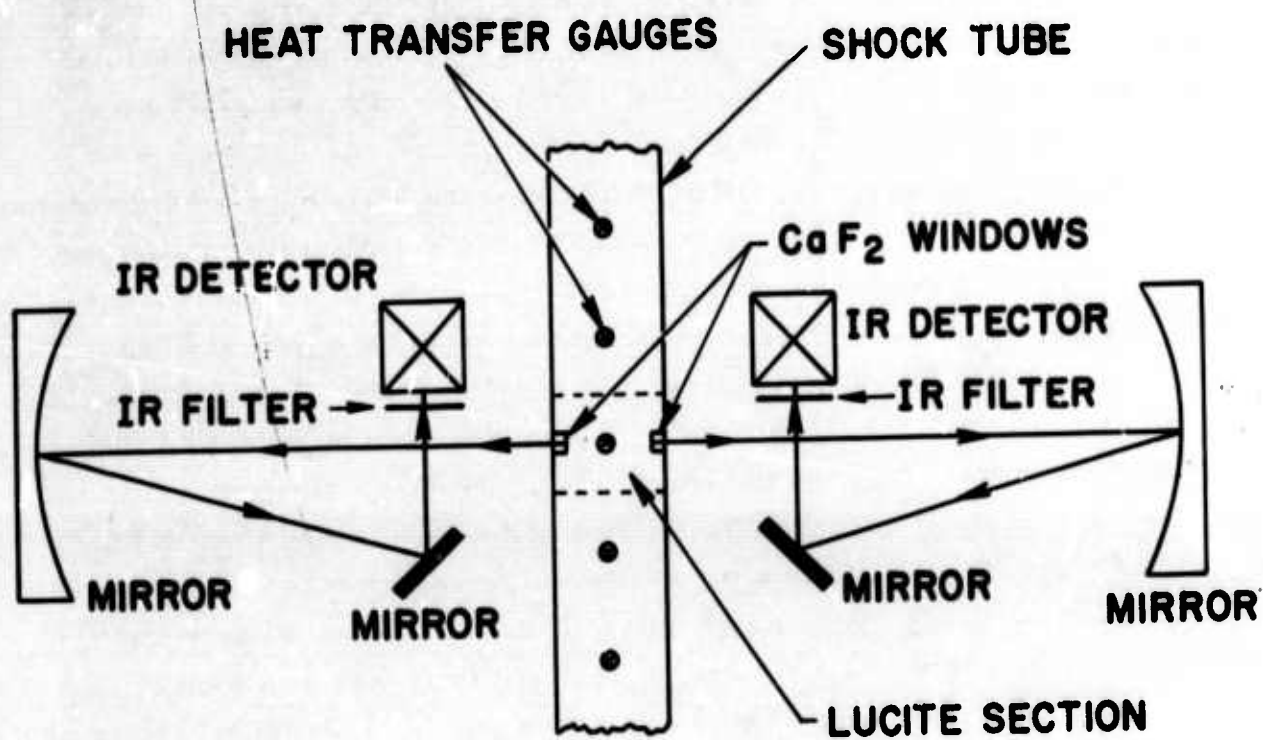


Fig. 4 Schematic diagram of shock tube section with infrared detection systems.

diaphragm, was made of lucite, a poor infrared reflector. At 5 microns wavelength, lucite is opaque with less than 5% reflectivity. In the initial runs, metal walls were used, but they gave extraneous signals due to reflected radiation originating downstream of the window. Two infrared optical systems were located in the same plane normal to the shock tube axis. The detector in each system was imaged on the inner surface of the  $\text{CaF}_2$  infrared window with an 8 inch diameter, 10 inch focal length spherical mirror set at approximately unit magnification. An infrared filter was placed in front of each detector to isolate the band. The  $\text{CaF}_2$  infrared windows were radiused to the inside diameter of the shock tube. System I, used for good spatial resolution, had a 1 inch by 8 inch lucite aperture over the mirror, the narrow dimension being along the axis of the shock tube. The 1 mm by 5 mm active area of the (Philco) InSb infrared detector defined the image size with the 1 mm width imaged along the axis of the shock wave. There were no slits at the shock tube. Measurements with this InSb detector required rise time corrections when the signal rise time was faster than four microseconds. For the low shock velocity runs, System II used the entire mirror area and a 5 mm diameter (Philco) InSb infrared detector. This system has the maximum sensitivity and was used to investigate the impurity level and the initial NO low level signals. For the high shock velocities, the aperture on the mirror was reduced to 1" by 8" and a (Westinghouse) Ge: Au detector with a 1mm by 3mm effective sensitive area and with 0.7 microsecond overall system rise time was used. The outputs of the infrared detectors were fed directly to standard low noise high gain electronics and then displayed on oscilloscopes.

Figure 5 shows the spectral response of the InSb and Ge: Au detectors and the interference filters used in the experiment.

In most of the shock tube runs, the initial gas was room air passed through an ascarite filter and a liquid nitrogen trap to remove  $\text{H}_2\text{O}$  and  $\text{CO}_2$ . A series of check runs in synthetic air made from Matheson high purity  $\text{N}_2$  and  $\text{O}_2$  showed no difference in results when dried room air was used. The  $\text{H}_2$  used in the driver was replaced by He and a series of runs were repeated. The purpose of these runs was to ensure that

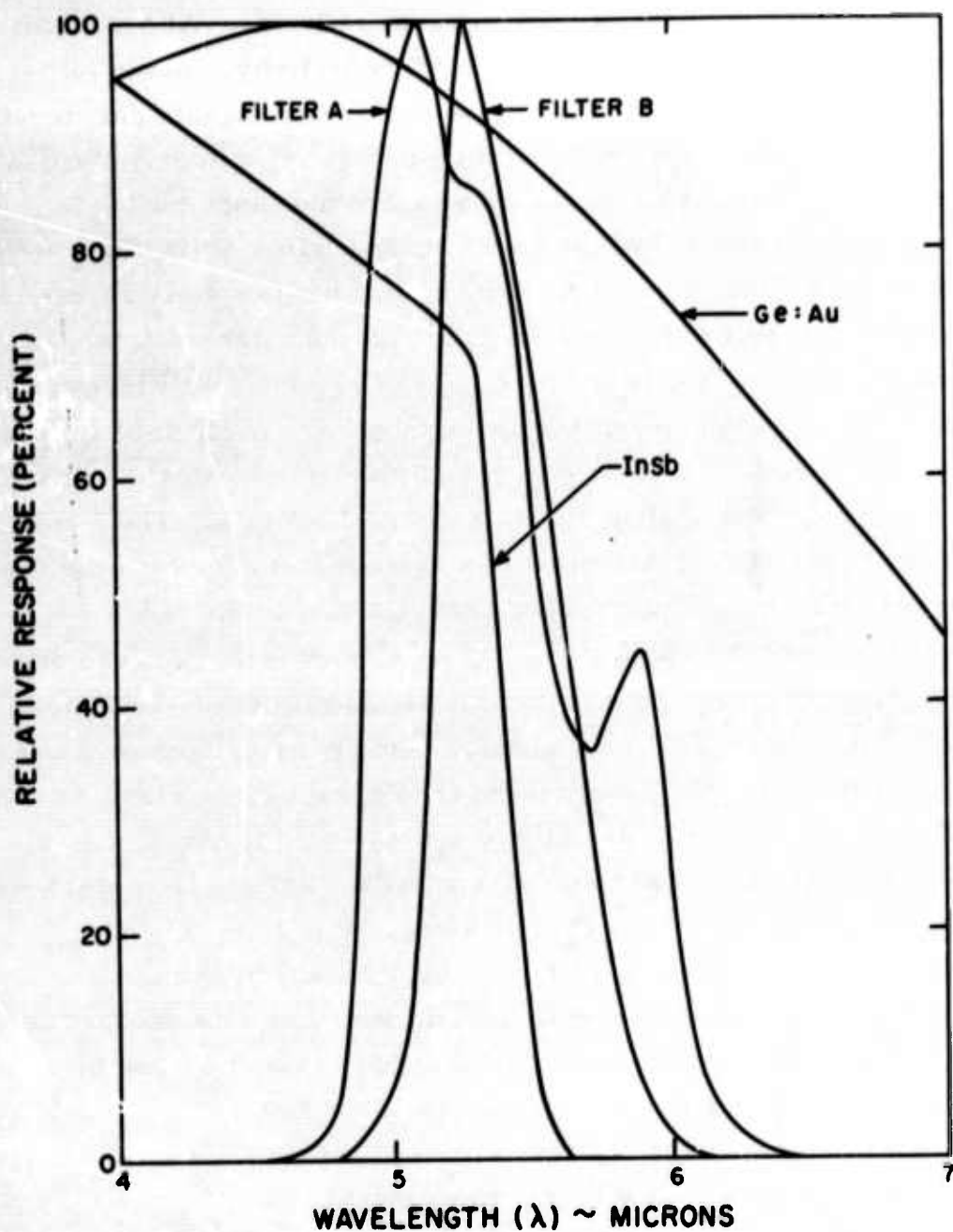


Fig. 5 The relative response for indium antimonide and gold-doped germanium infrared detectors as a function of wavelength. The relative transmittance of the filters used in the experiment is also shown as a function of wavelength. The curve for the gold-doped germanium detector was supplied by the manufacturer; the other curves were obtained from laboratory measurements.



hydrogen compounds from the previous run, that might be produced in the mixing region and deposited on the walls of the shock tube, would not contribute to the infrared emission. There were no detectable differences using the H<sub>2</sub> or He driver. Another series of runs was also made in pure N<sub>2</sub> and O<sub>2</sub> to check for infrared emission from impurities in these gases, and from boundary layer impurities such as lucite ablation products. For the N<sub>2</sub> and O<sub>2</sub> runs, only System II with the 5 mm diameter InSb detector showed a small signal, while System I, eight times less sensitive had no indication above noise. The signals remained relatively constant with shock velocity using either N<sub>2</sub> or O<sub>2</sub>. This radiation might have been due to boundary layer effects or impurities in the gases; the intensity was the equivalent to NO radiation from a  $2 \text{ to } 4 \times 10^{-4}$  NO concentration. These signals could be increased by increasing the shock tube base pressure to several microns Hg before filling the shock tube. This increased signal was consistent with about 10 ppm of water vapor.

#### Infrared System Calibration

The output signal from the infrared system was calibrated to give the NO concentration in the shock tube. In a series of shock tube runs using NO-Ar mixtures the NO infrared signal was determined as a function of the NO temperature, concentration and partial pressure. Figure 6 shows data oscillograms for 1, 10 and 100 percent NO in Ar runs. The voltage of the level portion (after either NO vibrational relaxation or system response time) normalized to 1 torr NO partial density is plotted as a function of the temperature in Fig. 7.

The curve in Fig. 7 is the calculated NO emission using Eq. (B-12) which assumes an optically thin gas; that is, the contribution from each molecule is additive. The height of the curve was adjusted for the best fit to the data. Note the excellent agreement with the computed curve except for the runs with 100% NO at an initial pressure of 5 torr, which are about 30% low. This decrease is due to self-absorption effects in which the center of the lines become black. For the shock tube runs in air, the partial pressure of nitric oxide behind the shock is less than 1/50 this value. In addition, there is pressure broadening by O<sub>2</sub> and N<sub>2</sub>. Thus, the air data does not

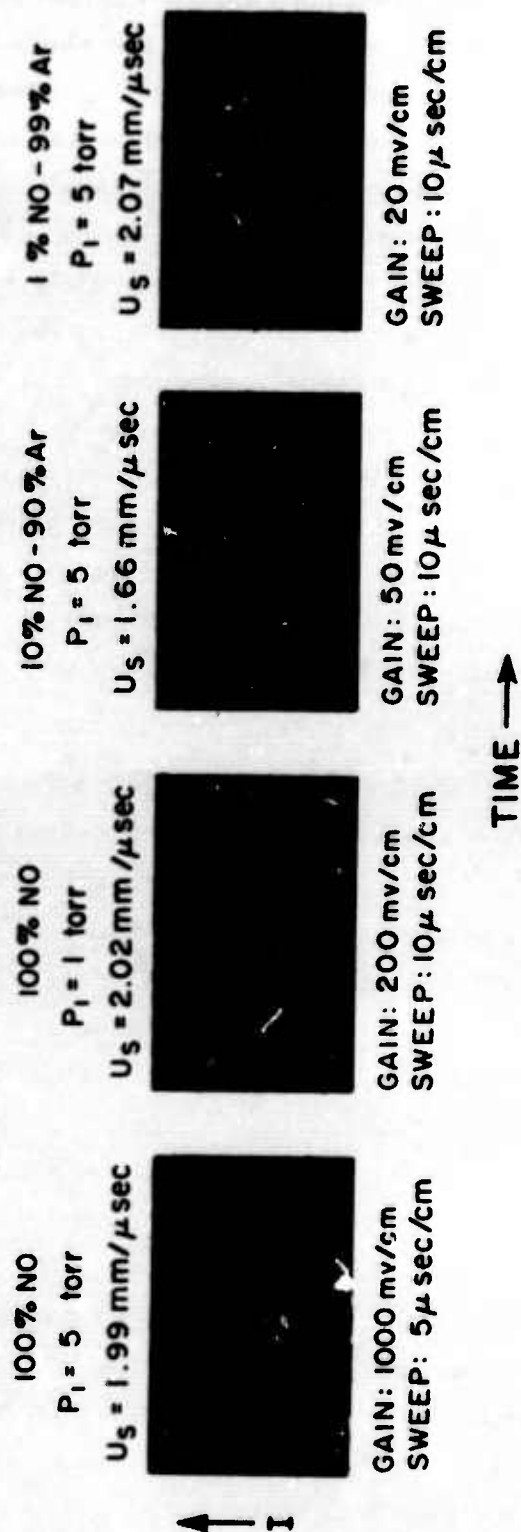


Fig. 6 Representative oscillograms showing the 5 micron band calibration data.

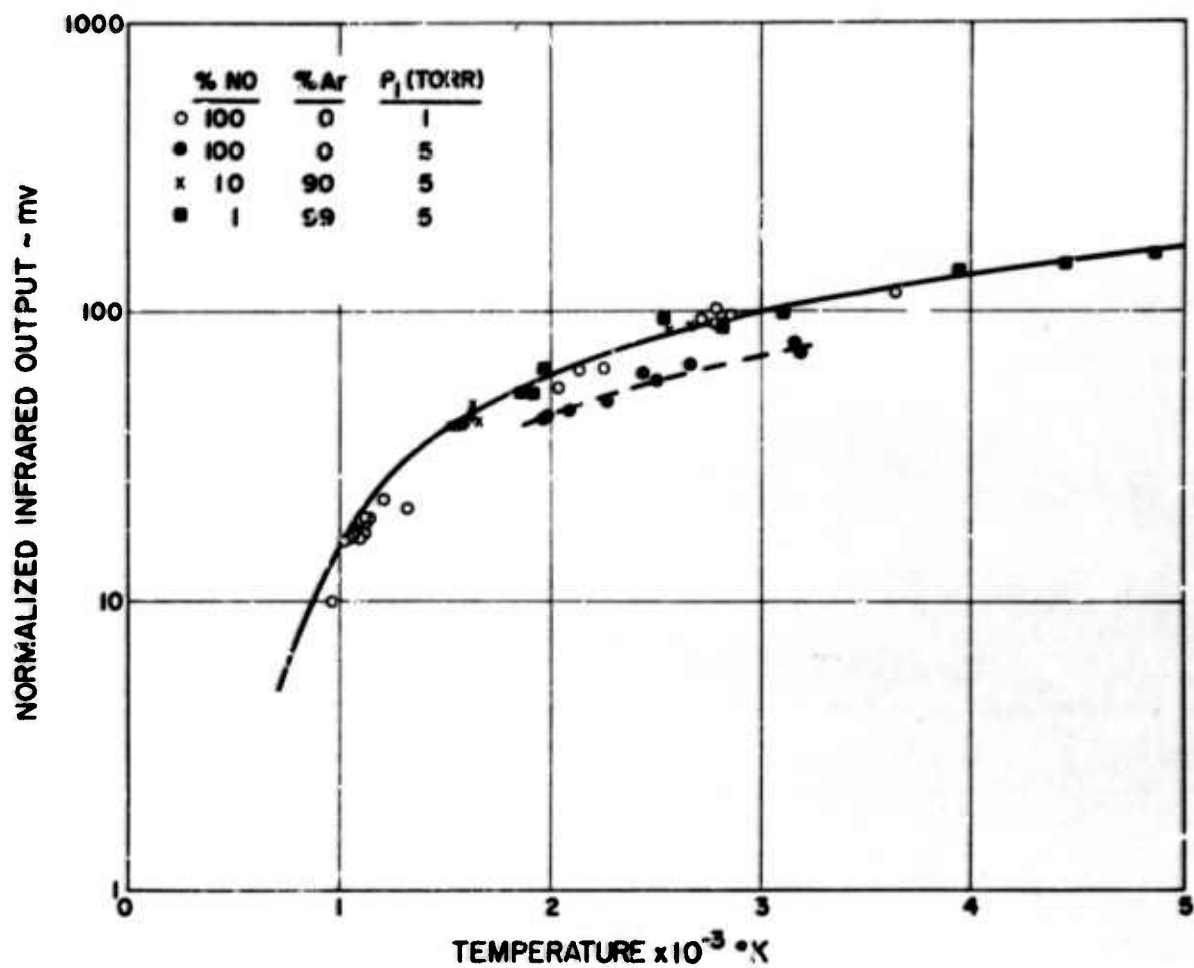


Fig. 7 NO infrared emission as a function of temperature. The solid curve shows the computed intensity variation with temperature assuming the weak line approximation. The data was normalized at (1/760) STP.



require corrections for self-absorption; the infrared emission is proportional to NO concentration with the temperature dependence given in Fig. 7, see also Appendix B.

The infrared systems were also calibrated and checked periodically with a black body light source. The primary purpose of the calibration was to ensure that there were no changes in the sensitivity during the experiment. A portion of the shock tube was replaced with a black body at 500°C. A chopper wheel in front of the source furnished an AC signal. In order to vary the energy incident on the infrared detector, apertures were placed over the focusing mirrors, always keeping the black body temperature at 500°C. This checked the linearity of the systems, and furnished signals with the same range of intensity as in the shock tube runs.

Figure 8 shows the black body calibration signal as a function of the exposed fraction,  $X$ , of the mirror area. The data reproduced to within 10% over the experimental period. This calibration is for System I with the InSb cell and filter B. Similar calibrations were obtained for the other systems.

#### NO Fundamental Band Intensity

The band intensity of the 5.3 micron NO fundamental band can be determined from the equilibrium NO emission measurements presented in Fig. 7. The previous discussions showed that the gas was optically thin. Thus, we can use the formulas developed in Appendix B. We start with Eq. (B-12) which gives the band emission coefficient  $c_{em}$  as a function of the NO emission,  $S$ , and the black body emission,  $S_B$ ,

$$c_{em} = \left( \frac{S}{S_B} \right) \left( \frac{x}{x_0} \right) \left( \frac{1}{N\ell} \right) \left\{ \frac{\sigma \tau I_b d\nu}{\sum_{v'} \sum_{j'} \dots} \right\} \quad (B-12), \quad (12)$$

Numerical values of the spectral and temperature dependence for the bracketed factor are presented in Fig. B-1. Use of the ratio  $S/S_B$  eliminates the need to determine the optical solid angle and the absolute magnitude of the filter transmission,  $\tau$ , and detector sensitivity,  $\sigma$ .

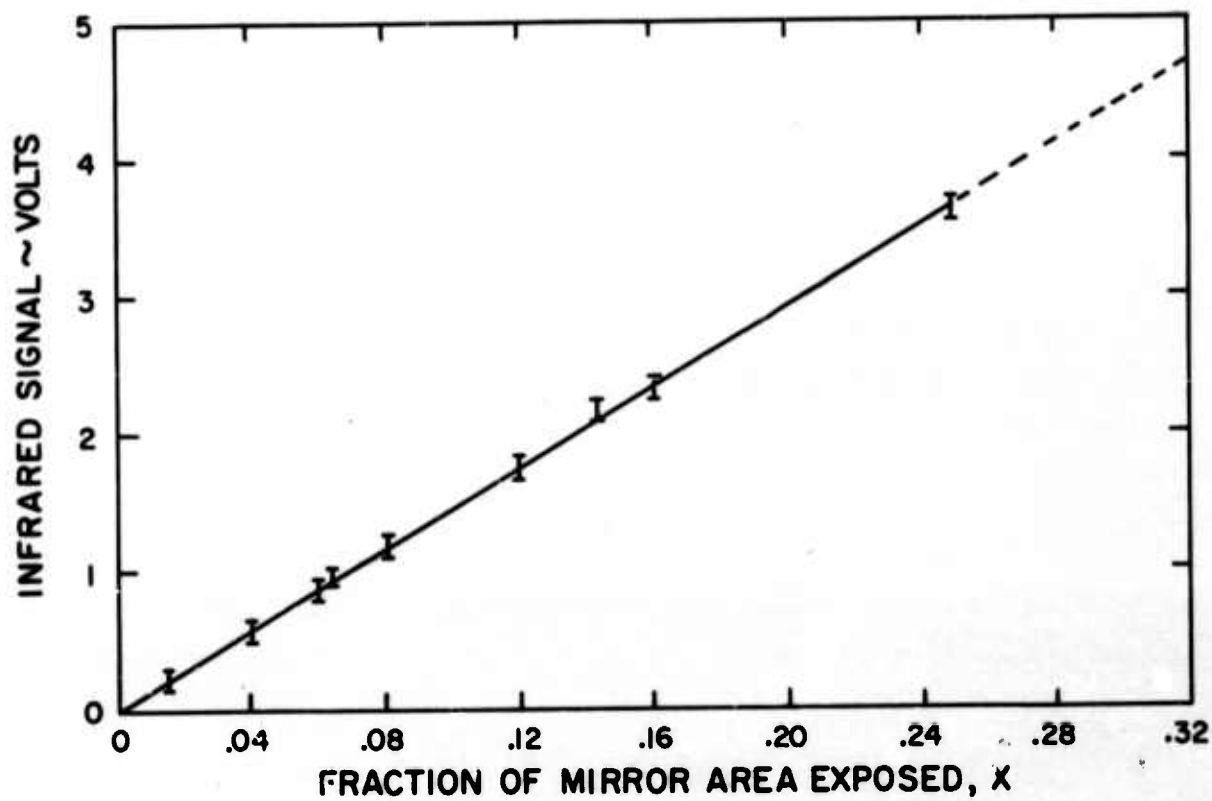


Fig. 8 The static calibration of the infrared recording system is accomplished by replacing the shock tube with a 500°C black body and varying the area of the collecting mirror. The observed signal is plotted as a function of the fraction of the mirror area uncovered.

To illustrate how Eq. (12) is used, we will determine  $c_{em}$  with the data at 3000°K. From the data shown in Fig. 7,  $N = 3.6 \times 10^{16}$ .  $X_0 = 1/2 \pi$ ,  $l = 3.81$  cm, and  $S = 100$  mV at 3000°K. From Fig. 8,  $(S_B/X) = 1.45 \times 10^4$  mV. The value of the bracketed factor at 3000°K is  $9.25 \times 10^{-8}$ , see Fig. B-1. Inserting these values into Eq. (12),  $c_{em}$  becomes

$$c_{em} = \frac{(10^2)}{(3.81)} \frac{(2\pi)(9.25 \times 10^{-8})}{(1.45 \times 10^4)(3.6 \times 10^{16})} = 2.96 \times 10^{-26} \frac{\text{ergs/sec}}{\text{part-ster}} \text{ cm}^4 \quad (13)$$

$c_{em}$  was calculated using the data in Fig. 7 by a least squares fit to Eq. (12).

$$c_{em} = (2.97 \pm 0.4) \times 10^{-26} \text{ (statistical error)} \quad (14)$$

This uncertainty is due to the scatter of the NO emission data. In addition, we have considered the systematic errors listed in Table II. The overall uncertainty in  $c_{em}$  due to systematic errors is 15%. Combining the systematic errors and the statistical variance, the overall error becomes

$$c_{em} = (2.97 \pm 0.54) \times 10^{-26} \frac{\text{ergs/sec}}{\text{particle-ster}} \text{ cm}^4 \quad (15)$$

The NO band intensity can be obtained directly from the emission coefficient. The band intensity is defined as the integral band absorption of an optically thin gas normalized to 1 cm<sup>3</sup> of NO at standard temperature and pressure. In terms of  $c_{em}$ , the band intensity becomes<sup>15</sup>

$$\int_{\text{band}} \mu dv = \frac{N_0 \nu_1 c_{em}}{2 hc^2} \quad (16)$$

$\nu_1 = 1876 \text{ cm}^{-1}$ , is the wave number at the center of the band;  $h$  = Planck's constant,  $c$  = velocity of light and  $N_0 = 2.69 \times 10^{19}$  (Loschmidt's Number). Inserting our value for  $c_{em}$ , the band intensity becomes

TABLE II  
SYSTEMATIC ERRORS

Source	Type	Value	$c_{em}$ Uncertainty
Black Body	Temperature	$\pm 2.5^{\circ}\text{C}$ at $500^{\circ}\text{C}$	} 2%
Black Body	Emissivity	$\pm 1\%$ at 99%	
Calibration Mirror	Reflectivity	3%	<1%
Filter	Spectral Response	<0.2%	<1%
Filter	Transmittance	3%	4%
Detector	Spectral Response	<1%	<12%
Detector	Relative Amplitude	<5%	<7%

$$\int_{\text{band}} \mu dv = 124 \pm 22 \text{ atm}^{-1} \text{ cm}^{-2}. \quad (17)$$

The values of the  $5.3 \mu$  fundamental NO band intensity obtained by others are shown in Table III. These values fall into two groups -- (1) high values and (2) low values. The high values are in general agreement with the original work of Havens<sup>18</sup> who used the optical dispersion method, a simple and reasonably accurate way of determining the fundamental band intensity of a diatomic molecule. The work of Penner and Weber<sup>20</sup> was repeated by Varanasi and Penner<sup>26</sup> where the latter obtained a higher value. No explanation for the difference in the two reported values was presented. The low value obtained by Vincent-Geisse<sup>21</sup> is difficult to explain. Fukuda,<sup>25</sup> and Breeze and Ferriso<sup>27</sup> worked at intensity levels where the line centers were black and the weak line approximation was no longer valid. This would be an important correction and should have been considered in the reduction of their data.

#### NO Production in Shock Heated Air

We will now present the measurements of NO production in shock heated air. Only the "raw" uncorrected data is discussed in this section. Corrections and analysis of the data are presented in Section IV.

Measurements of NO production in shock heated air are shown in Fig. 9. The NO infrared emission is given as a function of laboratory time for several shock velocities in the range of 2.28 to 4.02 mm/ $\mu$  sec and at pressures of 1, 5 and 50 torr. The shock heated gas conditions for the range of air data are presented in Figs. 1, 2 and 3. The infrared signal shows an initial incubation period with a low voltage level; it then rises rapidly to a peak value. At shock velocities below 2.6 mm/ $\mu$  sec the infrared signal rises monotonically, while at higher velocities the NO concentration peaks above equilibrium and approaches equilibrium from

TABLE III

## INTENSITY MEASUREMENTS FOR THE FUNDAMENTAL BAND OF NO

Values shown are referred to density at STP

Author	Method	Intensity $\text{cm}^{-2}\text{atm}^{-1}$
Havens (1938) <sup>18</sup>	Optical Dispersion	121
Dinsmore (1949) <sup>19</sup>	Zero Path Extrapolation	$145 \pm 29$
Penner and Weber (1953) <sup>20</sup>	Pressure Broadening	$70 \pm 7$
Vincent-Geisse (1954) <sup>21</sup>	Line Shape	82
Schurin and Clough (1963) <sup>22</sup>	Self Broadening	$111 \pm 7$
James (1964) <sup>23</sup>	Line Shape	$138 \pm 6$
Breeze and Ferriso (1964) <sup>24</sup>	Integrated Emission	$76 \pm 7$
Fukuda (1965) <sup>25</sup>	Integrated Emission	70 to 77
Ford and Shaw (1965) <sup>26</sup>	Integrated Absorption	$115 \pm 12$
Abels and Shaw (1966) <sup>27</sup>	Line Shape	$122 \pm 6$
Varanasi and Penner (1966) <sup>28</sup>	Pressure Broadening	$128 \pm 10$
This Experiment	Integrated Emission	$124 \pm 22$



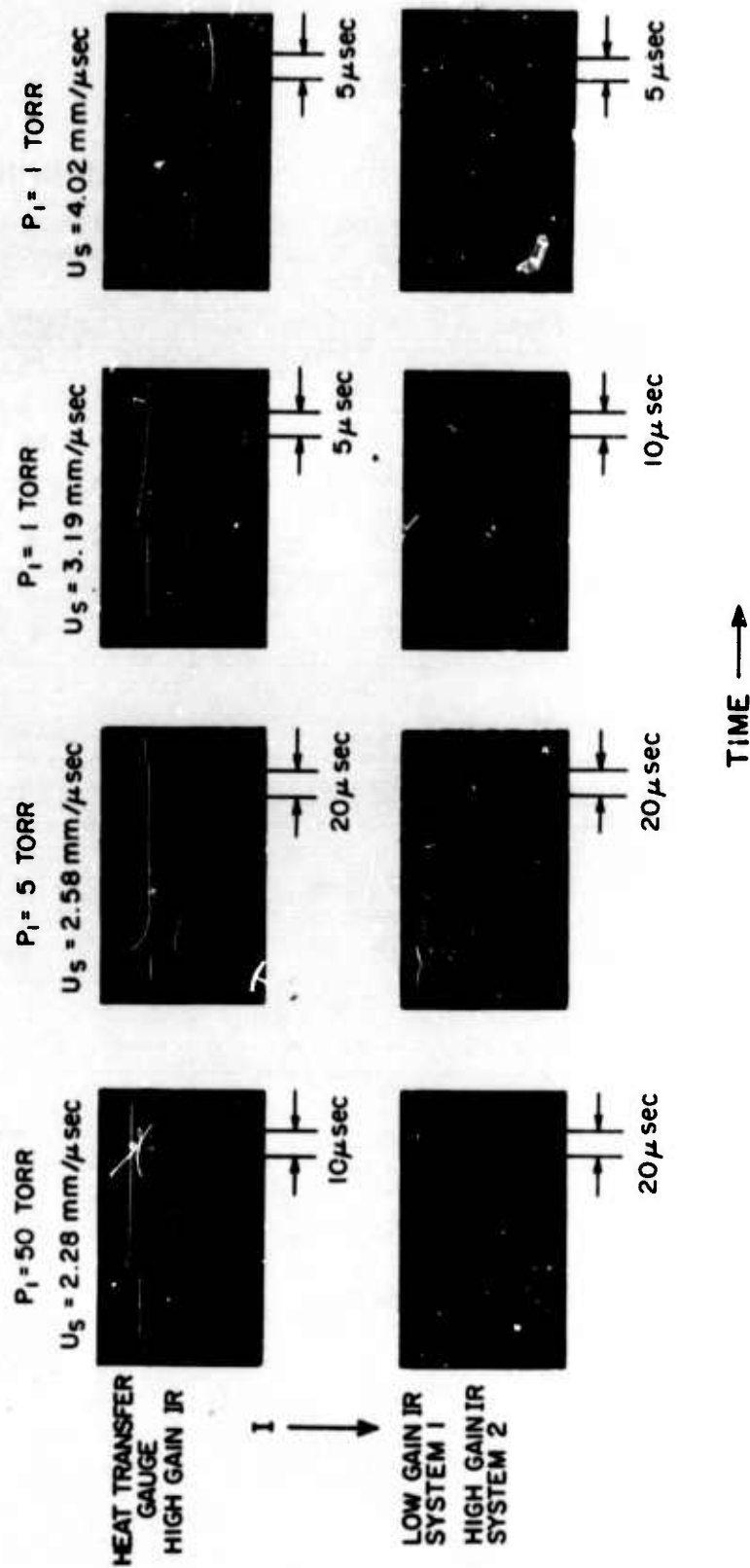


Fig. 9 The NO infrared emission in shock heated air for several conditions. The heat transfer gauge indicates the time of shock wave passage.

above. Figure 10 indicates features of the data to be analyzed: (1) the incubation time, (2) the time to reach  $1/4$ ,  $1/2$  and  $3/4$  the peak intensity, (3) the NO concentration at peak intensity. Only qualitative analysis was performed on the data after the peak intensity because of the uncertain corrections due to the effects of the side wall boundary layer and shock attenuation.

The incubation time may be defined in two ways: (1) the time at which a tangent to the fast rising portion intersects the zero level, and (2) the time at which the infrared signal becomes larger than the background level. Essentially the same incubation time is obtained using either definition. Figure 11 shows the observed incubation (laboratory) time as a function of incident shock velocity. The data were binary scaled to an initial pressure of 5 torr by multiplying the observed time by  $(P_1/5)$ , where  $P_1$  is the initial pressure in torr. The data show that the incubation time has bimolecular scaling. The solid curves show the  $N_2$  vibrational relaxation time in pure  $N_2$ <sup>29</sup> and in air.<sup>30</sup> The possible connections between the incubation time and the  $N_2$  vibrational relaxation time are discussed in the next section.

The NO mole fraction at the incubation time as determined from the infrared signal is shown in Fig. 12. As mentioned above, at this time the infrared signal becomes larger than the background signal, corresponding to a NO mole fraction of  $2$  to  $4 \times 10^{-4}$ . Also shown in Fig. 12 is the predicted mole fraction of NO using the reaction mechanisms and rate constants given in Table I.<sup>4</sup> For shock velocities below  $2.4 \text{ mm}/\mu \text{ sec}$  the data is consistent with the predicted NO production. However, by  $3.0 \text{ mm}/\mu \text{ sec}$  there is over an order of magnitude difference. This difference in the early NO production is the only major discrepancy between our experimental data and predictions; and is due to the predicted extra NO production by the reaction  $N_2 + O_2 \rightarrow 2NO$ .

After the incubation period the infrared signal rises rapidly to the peak value. The time for the infrared signal to reach one-quarter peak height ( $\tau_{1/4pk}$ ), half peak height ( $\tau_{1/2pk}$ ) and three-quarters peak height ( $\tau_{3/4pk}$ ) are shown in Figs. 13, 14 and 15. The half peak intensity point is nearly half the peak NO mole fraction. The temperature is higher at the half peak point than at the peak, thus, the NO emission per molecule is larger. This



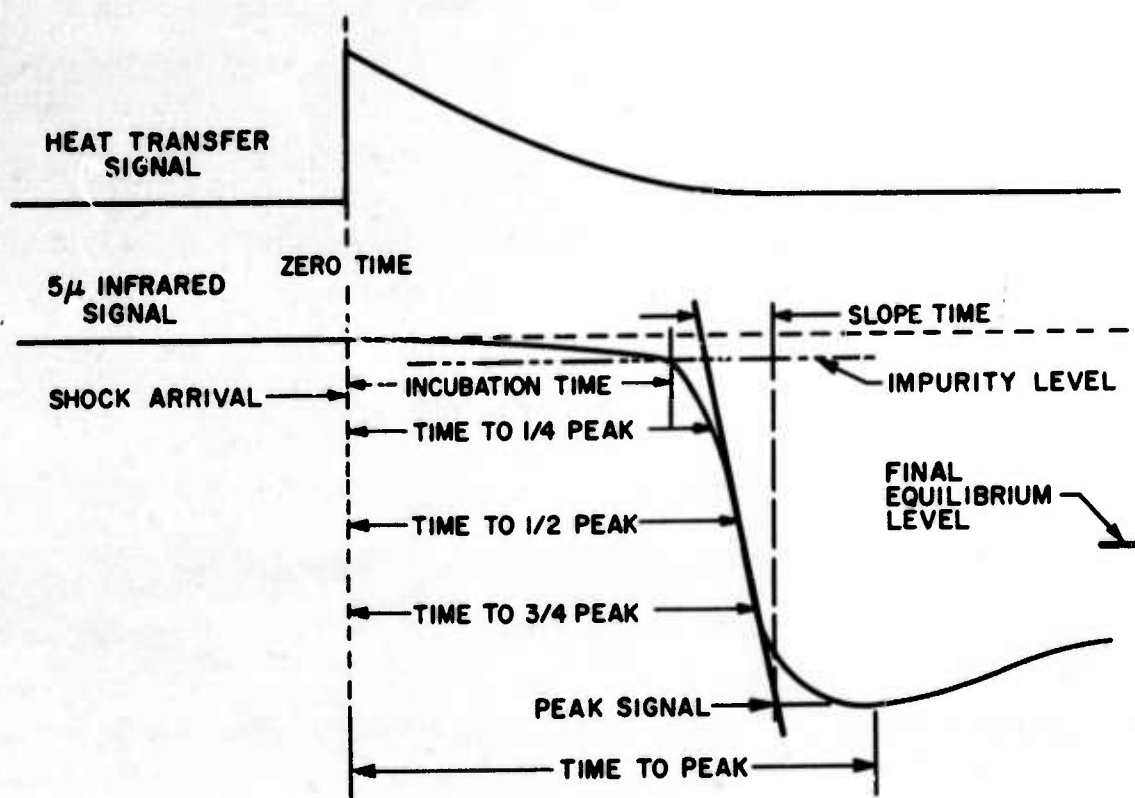


Fig. 10 Schematic drawing of the air data defining the various experimental measurements.

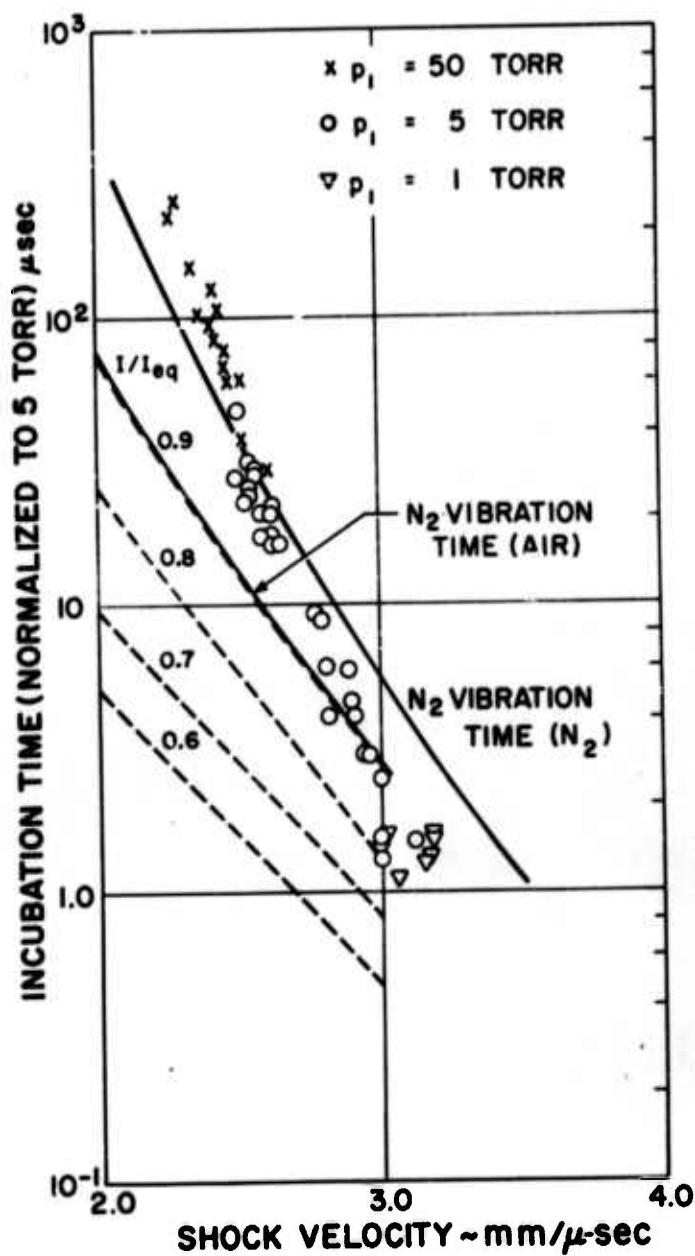


Fig. 11 Measured incubation time normalized binary to 5 torr initial pressure by bimolecular scaling. Solid curves use  $N_2$  vibrational times in pure  $N_2$  and air. Dashed curves, NO emission to that of vibration equilibrium emission ( $I/I_{eq}$ ).

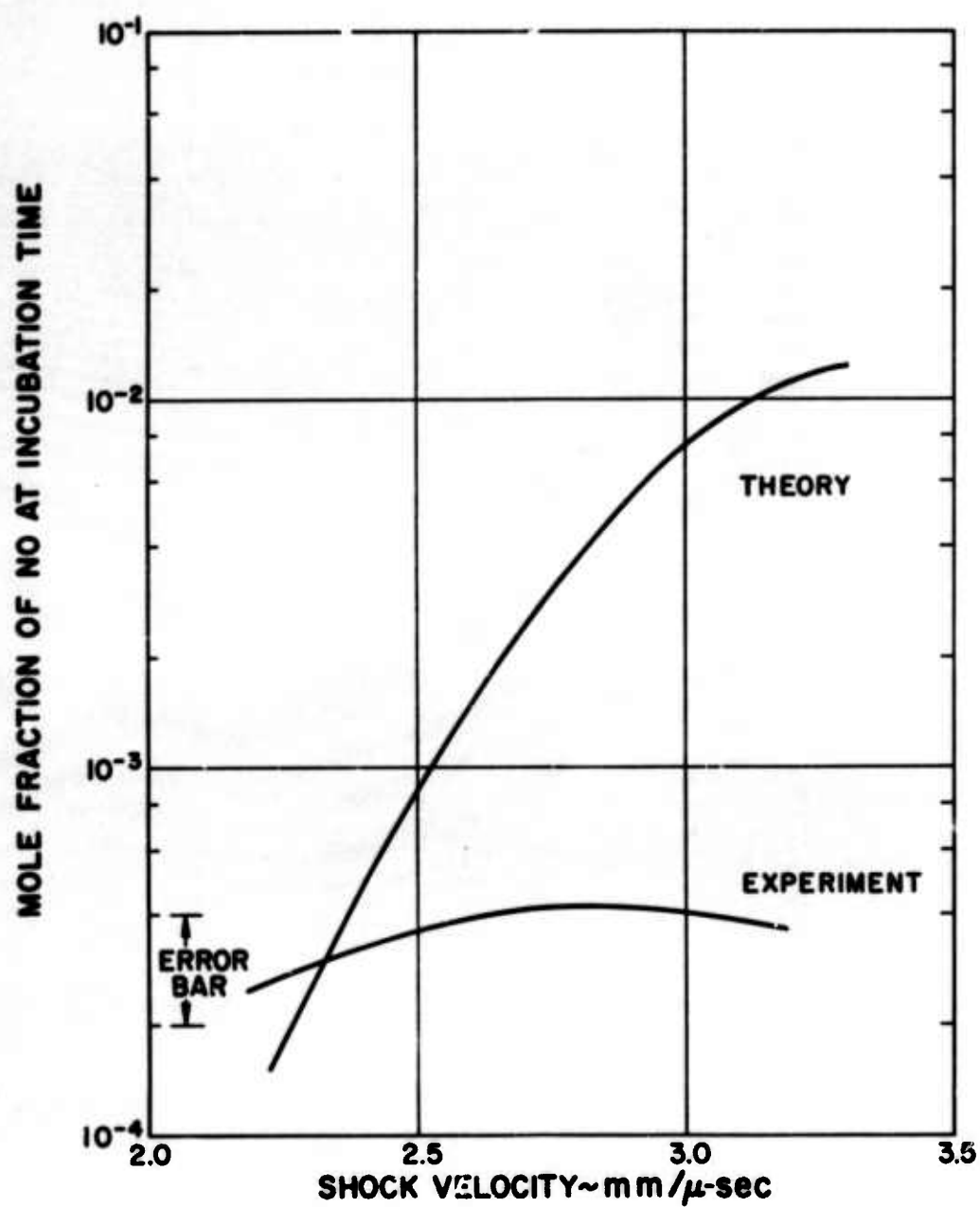


Fig. 12 Computed and measured NO mole fraction at the incubation time shown in Fig. 11.

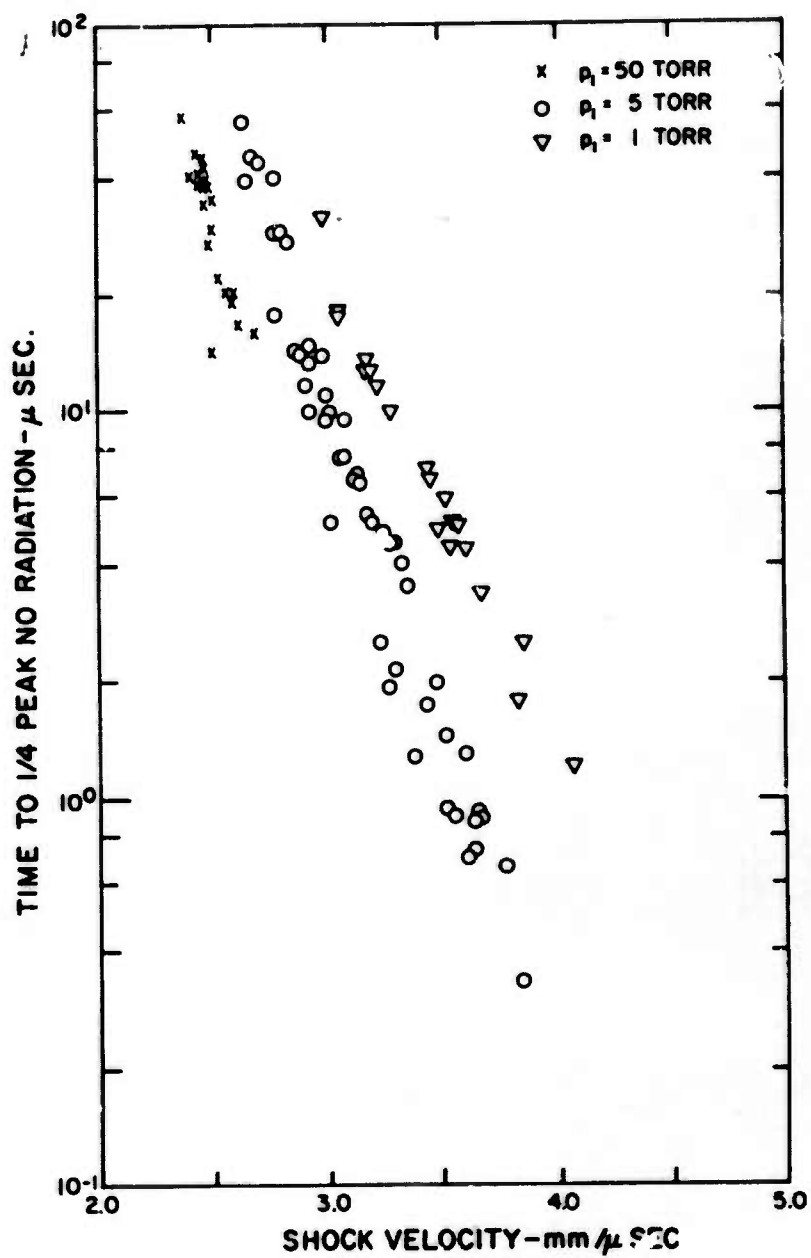


Fig. 13 Time for NO emission to reach 1/4 of the peak value. Data uncorrected for electronic response time.

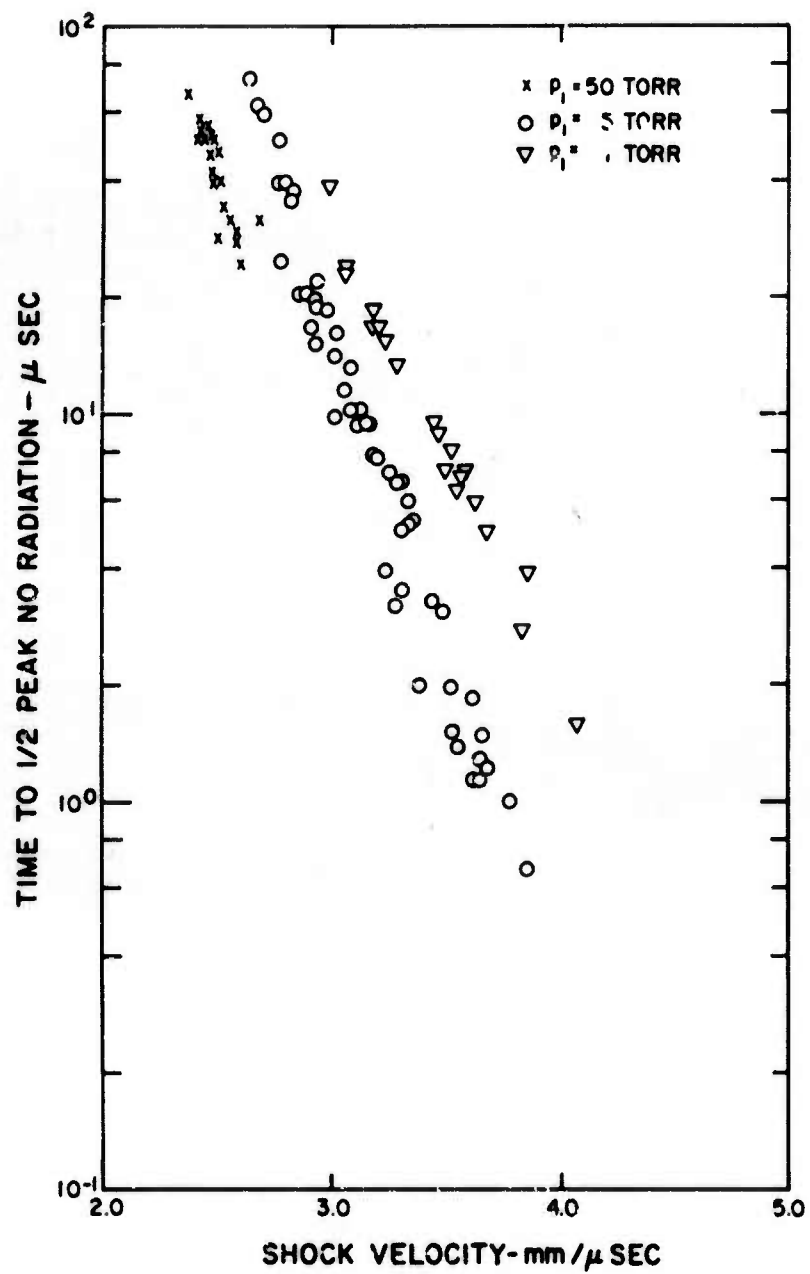


Fig. 14 Time for NO emission to reach 1/2 of the peak value. Data uncorrected for electronic response time.

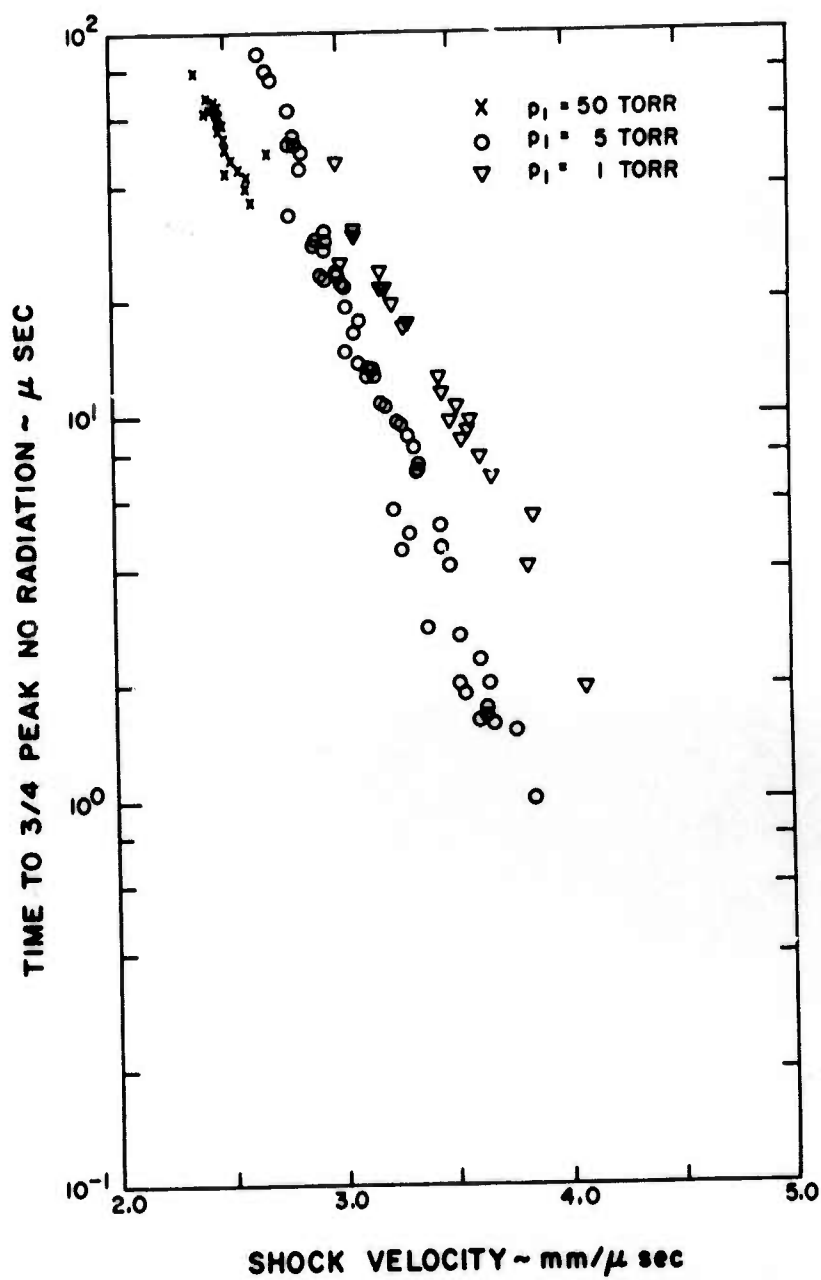


Fig. 15 Time for NO emission to reach 3/4 of the peak value. Data uncorrected for electronic response time.



increase is largely compensated by the lower density at the higher temperature. The measured time to reach the peak intensity is not presented because of the large uncertainty in estimating this time.

The peak infrared emission, presented in Fig. 16, can be correlated with the NO concentration. The NO emission calibration as a function of temperature is given in Fig. 7. The gas temperature at peak emission was not measured, but was obtained from computer calculations. Figure 17 shows the mole fraction of NO at the peak intensity. The curve shows the calculated peak value. This curve is independent of initial pressure for  $p_1 \leq 50$  torr, since 3-body reactions make a negligible contribution. The peak NO mole fraction is greater than that for chemical equilibrium (see Fig. 3), an effect predicted by Duff and Davidson,<sup>6</sup> which is due to local equilibrium between the molecules  $O_2$ ,  $N_2$  and NO through Reactions (2) and (3), while  $O_2$  dissociation proceeds at a slower rate through Reaction (4).

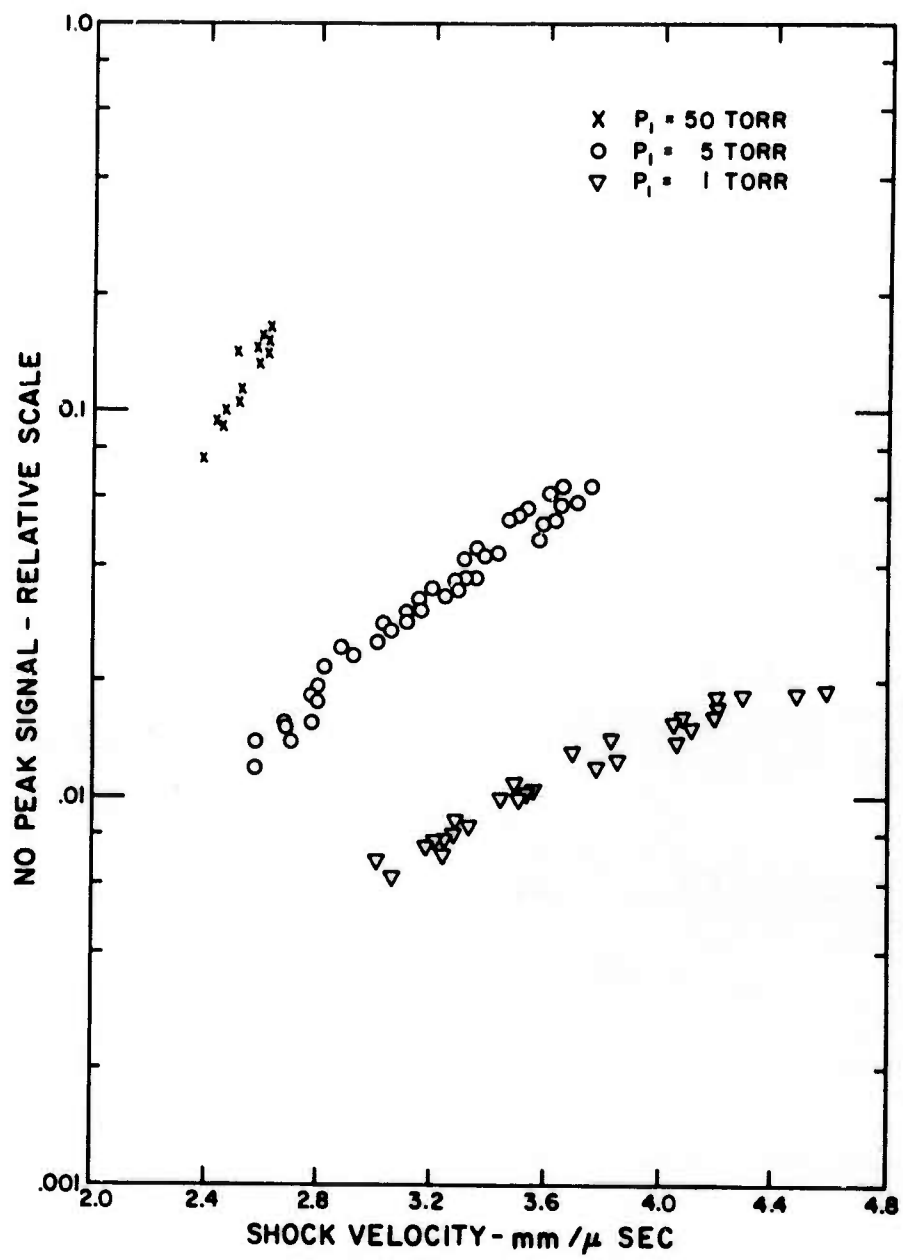


Fig. 16 NO peak signal as a function of shock velocity.

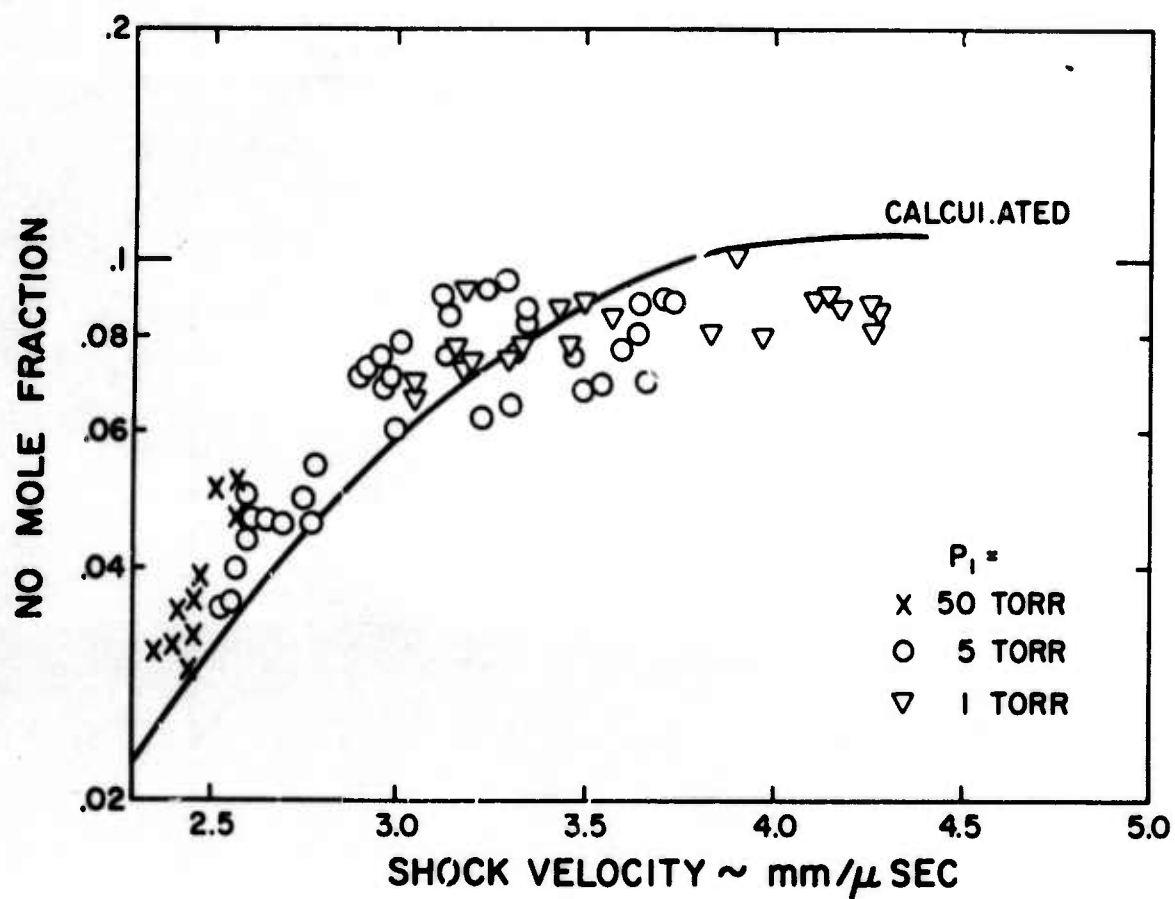


Fig. 17 The NO mole fraction at the peak intensity compared to calculations using the reactions and rate constants of Table I.

#### IV. DISCUSSION OF RESULTS

The experimental determination of the NO production rate in shock heated air will now be compared with computer calculations using the reaction mechanisms and chemical rates shown in Table I. The major difference between the experimental data and computer calculations is during the incubation period before the atom shuttle reactions become important, the measured NO radiation being much less than predicted, see Fig. 12.

Note that the incubation time occurs at approximately the  $N_2$  vibration relaxation time. While this might be a coincidence, it does suggest several reasons for the discrepancy. We have examined three possible reasons for this lack of agreement: (1) NO vibration lag reducing the infrared emission at early times; (2) wrong reaction rates in Table I, in particular Reaction (1)  $N_2 + O_2 \rightarrow 2NO$ ; and (3) coupling of vibration and chemistry in the reactions  $O_2 + N_2^* \rightarrow 2NO$  and  $O + N_2^* \rightarrow NO + O$ . The coupling effect assumes that the chemistry cannot proceed until  $N_2$  vibration approaches equilibrium conditions. First we will consider these three items and then return to a detailed comparison of data with calculations. It will be shown that NO vibration lag is unimportant, and that Reaction (1)  $N_2 + O_2 \rightarrow 2NO$  in Table I should be deleted. It is difficult to ascertain whether vibration and chemistry are coupled from the present data.

##### Vibrational Relaxation of NO

The NO concentration is determined from the 5.3 micron band intensity assuming the NO vibrational and translational temperatures are equal. To evaluate the limitations of this assumption, we must know the NO vibrational relaxation rates. During the incubation period, the NO concentration is low, thus the NO vibrational relaxation depends on collisions with  $O_2$  and  $N_2$ . If the NO- $N_2$  vibration-vibration exchange

were fast, NO would follow the  $N_2$  vibrational temperature. Since the NO infrared emission per molecule is an increasing function of the vibrational temperature, the radiation could be much less during the incubation period, until the  $N_2$  vibrational relaxation is complete.

The general problem of the vibrational excitation of a small amount of NO in  $O_2$ - $N_2$  mixtures is discussed in detail in Appendix A. For trace amounts of NO, NO is vibrationally excited by thermal collisions with  $N_2$  via the reaction  $N_2 + NO \rightarrow N_2 + NO^*$ .<sup>31</sup> In addition, vibrational energy transfer to  $N_2$  via the reaction  $NO^* + N_2 \rightarrow NO + N_2^*$  is slow enough,<sup>31</sup> so that the NO vibrational temperature was above that for  $N_2$  during the relaxation process. Figure 11 shows the calculated effects of the NO vibrational relaxation on the NO infrared emission. The dashed curves give the times at which the ratio of the infrared emission to the vibration equilibrium emission is 0.60, 0.70, 0.80 and 0.90. These curves were determined using the vibrational energy relaxation curves in Figs. A2-A4. Also shown in Fig. 11 are the incubation times. Note that at the incubation time the correction to the infrared emission due to vibration lag is less than 10% over the shock velocity range from 2.0 to 2.8 mm per microsecond. Thus, NO vibration lag does not account for the low infrared emission during the incubation period.

#### Wrong Rate Constant for $N_2 + O_2 \rightarrow 2NO$

A second possible reason for the lack of agreement during the incubation period is that the rate constant used for the reaction  $N_2 + O_2 \rightarrow 2NO$  is incorrect. This reaction produces most of the NO during the incubation time. If the rate were at least an order of magnitude smaller, then there would not be any disagreement. The rate constant used was suggested by Freedman and Daiber,<sup>11</sup> and Wray and Teare<sup>9</sup> who studied the reverse reaction and measured the decrease of NO in shock heated NO-Ar mixtures. They proposed the reaction  $2NO \rightarrow N_2 + O_2$  for the NO depletion; however, the reaction products were not observed. The alternate reaction<sup>14</sup>  $2NO \rightarrow N_2O + O$  could also account for the depletion of NO in shock heated NO. If this latter reaction were dominant, then the rate constant for Reaction (1) would be uncertain.

Several measurements on shock heated NO were made in order to check the reaction mechanisms proposed by Freedman and Daiber<sup>11</sup> and Wray and Teare.<sup>9</sup> In addition to measurements of the NO concentration, we observed atomic O and N<sub>2</sub>O. The NO and N<sub>2</sub>O concentrations were determined by the emission in the 5.3 and 4.6 micron bands, respectively. Atomic O was determined from the chemiluminescent reaction  $\text{NO} + \text{C} \rightarrow \text{NO}_2 + (h\nu)$ , by observing radiation in a band from 0.5 to 0.6 microns. The initial O production is directly proportional to this chemiluminescent radiation, since the initial NO concentration does not vary. Figure 18 shows some of the measurements of shock heated NO and NO-Ar mixtures. Note that N<sub>2</sub>O and O increase linearly with time, indicating directly the reaction  $\text{NO} + \text{NO} \rightarrow \text{N}_2\text{O} + \text{O}$ . Figure 19 shows the results of analyzing the initial decay of NO and the initial rise of O. The large error bars on the O data are due to incomplete calibration.

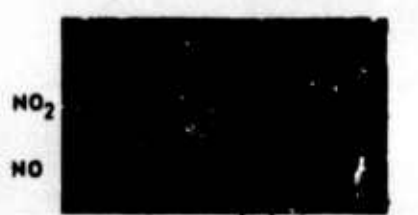
Note that both rates are essentially the same. The rate constant for the depletion of NO is equal to that for the increase in O, and also equal to that suggested by Freedman and Daiber,<sup>11</sup> the solid curve.

No observation of the products of the reaction  $2\text{NO} \rightarrow \text{N}_2 + \text{O}_2$  was made. The rate constant for this reaction is unknown, because it was not measured by Freedman and Daiber,<sup>11</sup> and Wray and Teare.<sup>9</sup> The initial slope of our shocked air data can be used to obtain an upper limit to this reaction which at 4000°K is  $< 0.10$  the rate given in Table I. For the purpose of air chemistry this rate constant is small enough so that Reaction (1) can be deleted.

#### Coupling of Vibration and Dissociation

A third reason for the discrepancy between prediction and observed initial NO production may be due to coupling between vibration and chemistry. The rate constants for Reactions (1) and (2) could depend on the vibrational temperature, and the expected rate constant would not be attained until N<sub>2</sub> vibrational equilibrium. Thus, Table I gives the rate constants for the reactions  $\text{O}_2^* + \text{N}_2^* \rightarrow 2\text{NO}$  and  $\text{O} + \text{N}_2^* \rightarrow \text{NO} + \text{N}$ , where N<sub>2</sub><sup>\*</sup> indicates equilibrium vibration. Previously we showed that the reaction  $\text{O}_2 + \text{N}_2 \rightarrow 2\text{NO}$  can be ignored; thus, we must investigate only the latter reaction for





TIME → 50 μSEC

SHOCK VELOCITY =  $2.07 \frac{\text{mm}}{\mu\text{sec}}$

INITIAL PRESSURE = 5 TORR

PURE NO

INITIAL SHOCKED TEMP. 2100 °K

(a)



TIME → 20 μSEC

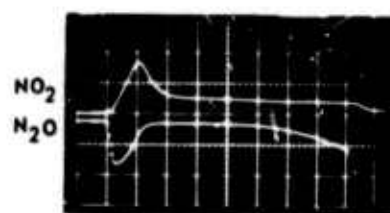
SHOCK VELOCITY =  $2.38 \frac{\text{mm}}{\mu\text{sec}}$

INITIAL PRESSURE = 10 TORR

PURE NO

INITIAL SHOCKED TEMP. 2700 °K

(b)



TIME → 20 μSEC

SHOCK VELOCITY =  $2.54 \frac{\text{mm}}{\mu\text{sec}}$

INITIAL PRESSURE = 10 TORR

PURE NO

INITIAL SHOCKED TEMP. 2900 °K

(c)

Fig. 18 Measurements of O and N<sub>2</sub>O production in shock heated NO. O determined by  $\text{O} + \text{NO} \rightarrow \text{NO}_2 + h\nu$  chemiluminescent reaction, NO and N<sub>2</sub>O concentrations by the 5.3 and 4.6 micron emission, respectively.

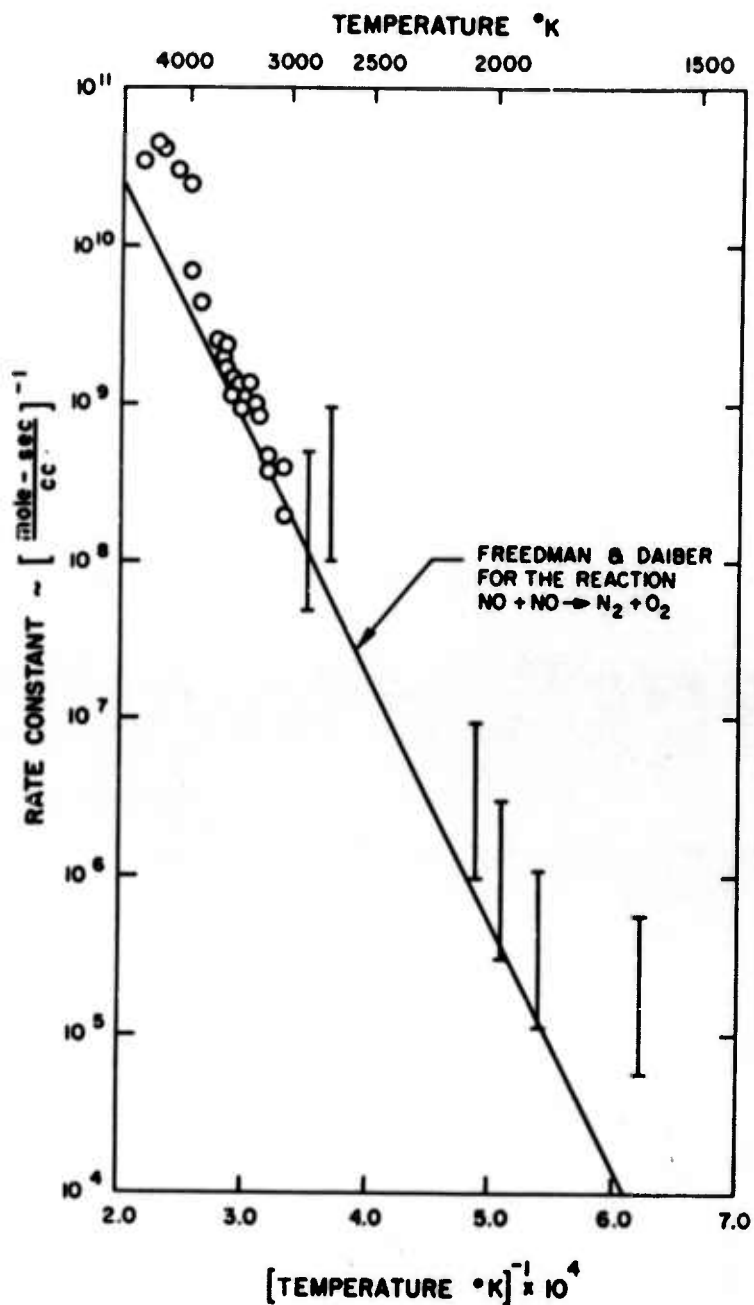


Fig. 19 Experimentally determined rate constant for the initial dissociation of NO, open circles, and production of atomic O, vertical bars. Curve gives Freedman and Daiber measured rate constant for NO depletion.

the effects of  $N_2$  vibration lag. The coupling of vibration and chemistry has been observed in  $O_2^{32}$  dissociation and a similar connection might occur here. The best place to check for the effect of the coupling is at the end of the incubation period by comparing the NO intensity at that time to the predicted value. Since the observed and predicted NO intensity is small at the incubation time, we cannot obtain information on vibration-dissociation coupling with the present data.

It is interesting to note that  $N_2$  has the slowest molecular vibration relaxation rate; thus, this reaction is ideally suited for studying vibration coupling to chemistry. The possibility of such coupling in Reaction (2) could be investigated experimentally, if initially an atomic O- $N_2$  mixture were used. This might be achieved with an initial  $O_3$ - $N_2$  mixture. Upon shock heating,  $O_3$  would quickly dissociate to  $O_2$  and O, thereby preparing an initial O concentration before the  $N_2$  vibration relaxation has progressed significantly. Under these conditions, without coupling, the NO production would increase linearly with time during  $N_2$  vibrational relaxation. However, with coupling, initially the chemical rate constant would be less and the NO formation would show an incubation.

#### Comparison of Computed and Experimental NO Chemistry

As described above, the chemical kinetics of NO production is a two-step process in which  $O_2$  is first dissociated, then the NO is formed in the atom shuttle reactions. The direct bimolecular Reaction (1) is deleted. In initial attempts to make a detailed comparison of the predicted radiation with the experimental data, the detailed fit was rather poor. Some preliminary estimates indicated the effects of shock velocity attenuation and boundary layer on the shock tube wall could not be ignored. A calculating procedure was developed which added the effects of the side wall boundary layer on the chemistry. Appendix C presents a detailed derivation of the computer program used.

Computer calculations are presented in Figs. 20, 21 and 22. The dashed curves show the computed times with the rates in Table I (bimolecular reaction omitted); the solid curves use a factor of 2.5 smaller rate constant for Reaction (2).

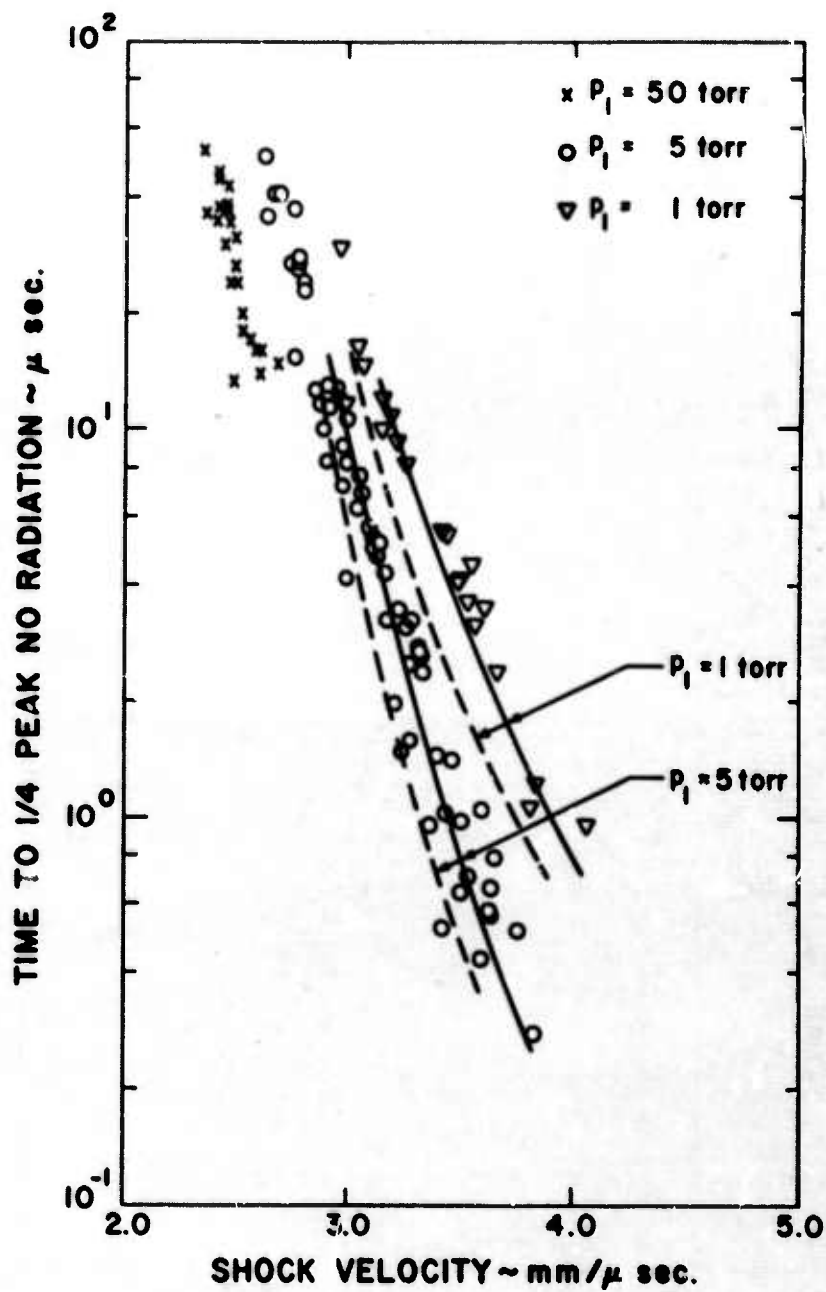
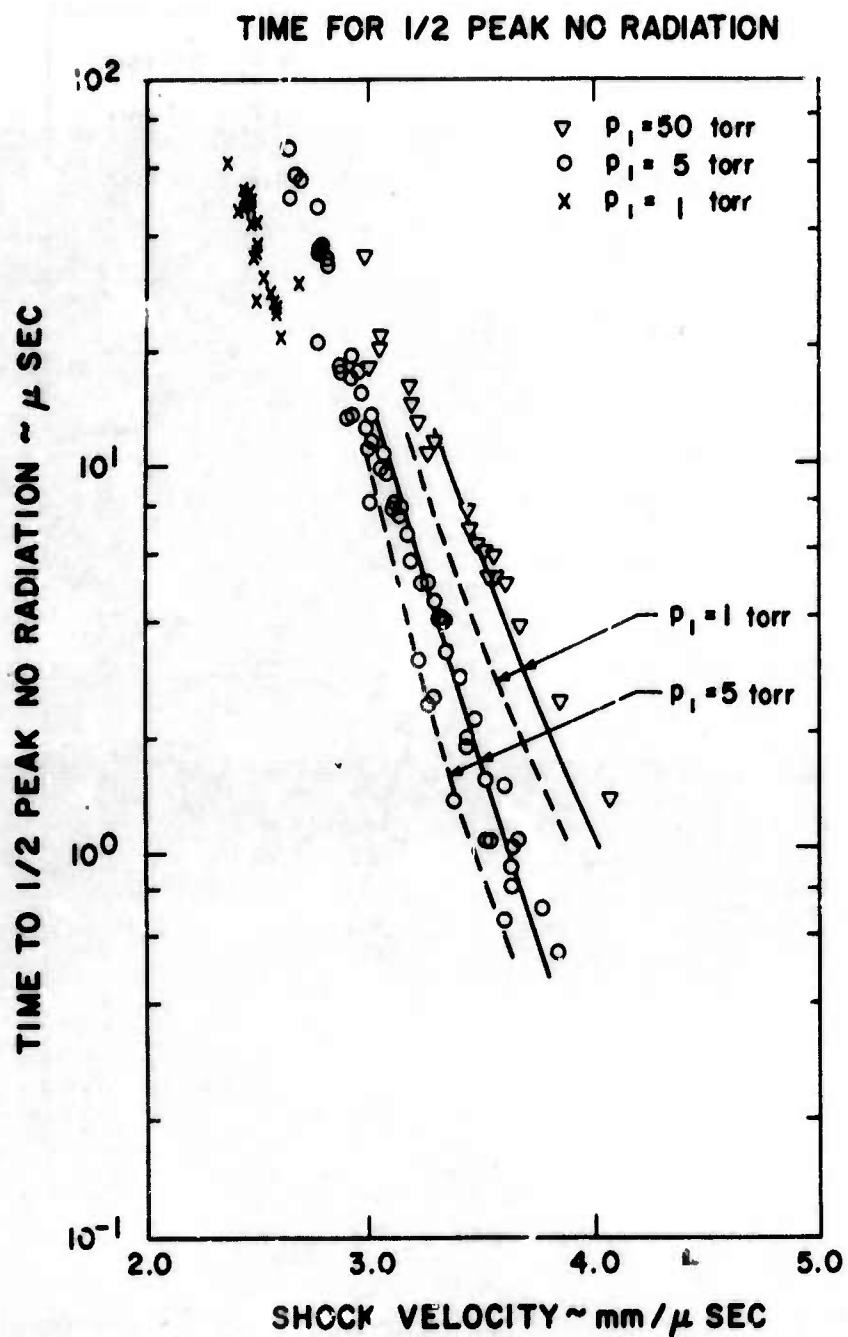


Fig. 20 Time to 1/4 peak NO emission corrected for electronic response time. The dashed curve uses reactions given in Table I with reaction 1 omitted. The solid curve uses a 2.5 times smaller value for  $k_2$ .



**Fig. 21** Time to 1/2 peak NO emission corrected for electronic response time. The dashed curve uses reactions given in Table I with reaction 1 omitted. The solid curve uses a 2.5 times smaller value for  $k_2$ .

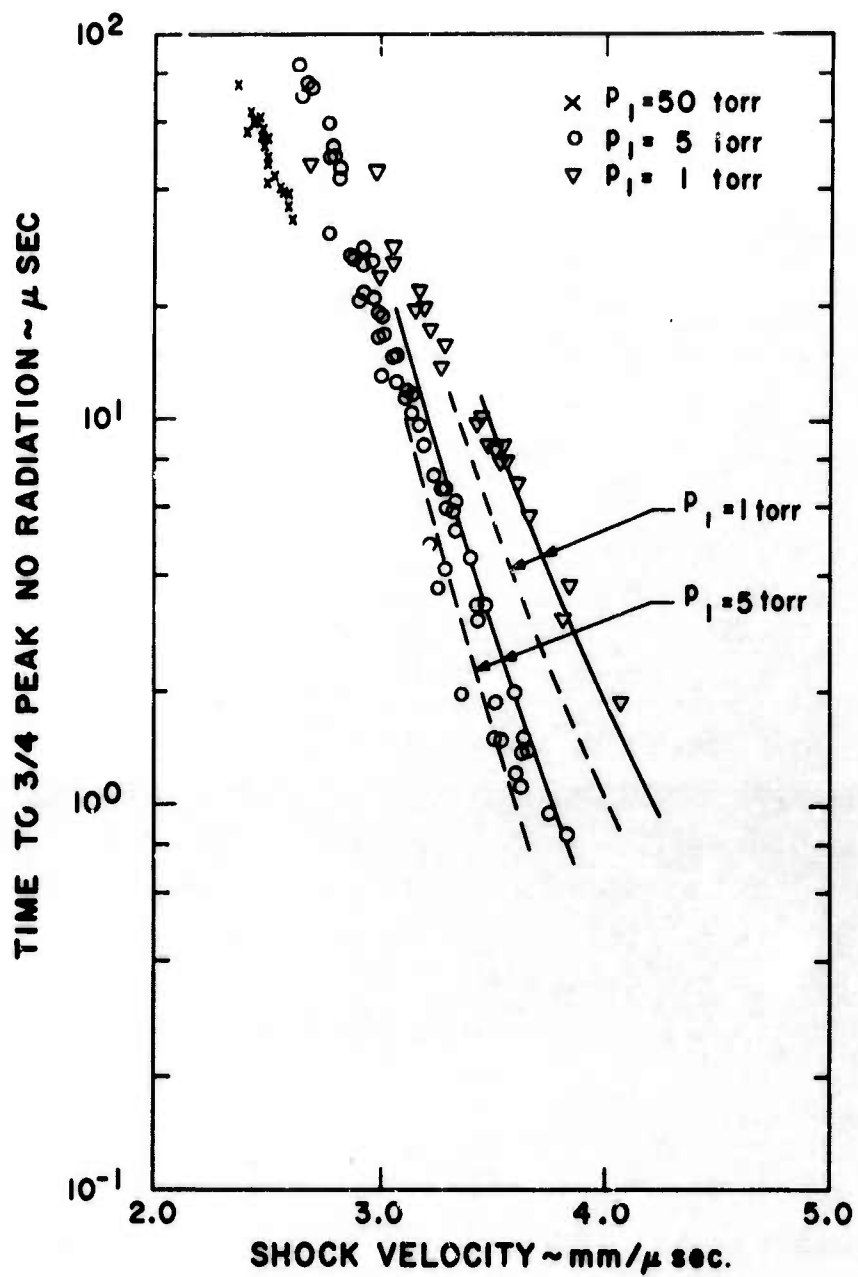


Fig. 22 Time to 3/4 peak NO emission corrected for electronic response time. The dashed curve uses the reactions given in Table I with reaction 1 omitted. The solid curve uses a 2.5 times smaller value for  $k_2$ .



The major correction to the experimental data is due to the finite electronic response time. The correction for electronic response time becomes significant at the higher shock velocities where the chemistry proceeds rapidly. Using the measured electronic response time  $\tau_e$  and assuming a simple RC circuit ( $\tau_e = RC$ ), then the correction to the data can be obtained from the relation

$$S_c = S + \tau_e (dS/dt) \quad (18)$$

$S$  is the observed signal output on the oscillogram trace, and  $S_c$  is the corrected signal. The value of  $\tau_e$  varied from 0.3 to 2 microseconds for different runs, the smaller value applying to the Ce: Au system. The data in Figs. 20, 21 and 22 have been corrected for the electronic response time. The change in the data due to electronic response time corrections can be obtained by comparing Figs. 20, 21 and 22 with Figs. 13, 14 and 15.

In Figs. 20, 21 and 22 the comparison of the solid curves with the data is quite good, except for times longer than 15 microseconds. At these times the corrections to the data due to shock velocity attenuation become important. Since we did not correct for this effect, the data at later times were not used for analysis. The solid and the dashed curves show computed times as a function of shock velocity and initial pressure with the rate constant  $k_2$  as a parameter. We used the following procedure for determining our experimental rate constant product for each of the experimental points. The NO concentration with time is obtained by integrating Reaction (2)

$$NO = \int_0^t 2k_2 [O][N_2] dt' \quad (19)$$

The factor of 2 is due to the additional NO production through Reaction (3).  $N_2$  is the original concentration, while  $O$  is produced by  $O_2$  dissociation

$$[O] = \int_0^t 2[O_2] \{k_{4,O_2}[O_2] + k_{4,N_2}[N_2] + k_{4,O}[O]\} dt'' \quad (20)$$

Inserting Eq. (20) into Eq. (19) and substituting the rate constant expressions from Table I, we obtain

$$[\text{NO}] = 4 [k_2^0 k_4^0] \int_0^t [\text{N}_2] \exp[-T_2/T] dt' \cdot \int_0^{t'} [\text{O}_2] \{2[\text{N}_2] + 9[\text{O}_2] + 25[\text{O}]\} \sqrt{T \left(\frac{T_4}{T}\right)^{3/2}} \exp[-T_4/T] dt'' \quad (21)$$

$T$  is the temperature;  $T_2 = 39,000^\circ\text{K}$  and  $T_4 = 59,000^\circ\text{K}$ , corresponding to the activation energies for Reactions (2) and (4), respectively.

$k_2^0 = 7 \times 10^{13}$  and  $k_4^0 = 2.5 \times 10^{11} \text{ cm}^3/\text{mole-sec}$  are the coefficients of the rate constant expressions for Reactions (2) and (4), respectively. The NO concentration is shown to be proportional to the product  $[k_2^0 k_4^0]$  in Eq. (21). For each shock tube run we measured three experimental times: at the occurrence of 1/4, 1/2 and 3/4 peak NO emission. Experimental values for  $[k_2^0 k_4^0]$  were determined from these time measurements in the following manner. The solid and dashed curves in Figs. 20, 21 and 22 are the computer calculated times for two different values of  $[k_2^0 k_4^0]$ . These times were related by the expression

$$[k_2^0 k_4^0]_s t_s^2 (1 + at_s) = [k_2^0 k_4^0]_d t_d^2 (1 + at_d) \quad (22)$$

where the subscripts  $s$  and  $d$  indicate values for the solid and dashed curves respectively. We then solved for  $a$ , the only unknown in Eq. (22), as a function of shock velocity. Each experimental time measurement was substituted in the expression

$$[k_2^0 k_4^0]_e t_e^2 (1 + at_e) = [k_2^0 k_4^0]_d t_d^2 (1 + at_d) \quad (23)$$

where the subscript  $e$  refers to experimental data. For a measured experimental time and shock velocity the only unknown quantity in Eq. (23) is  $[k_2^0 k_4^0]_e$ .

The ratio of the experimental rate coefficient product  $[k_2^0 k_4^0]_e$  to the rate coefficient product given in Table I  $[k_2^0 k_4^0]_d$  is plotted as a function of shock velocity in Fig. 23. Also shown are gas temperatures, obtained

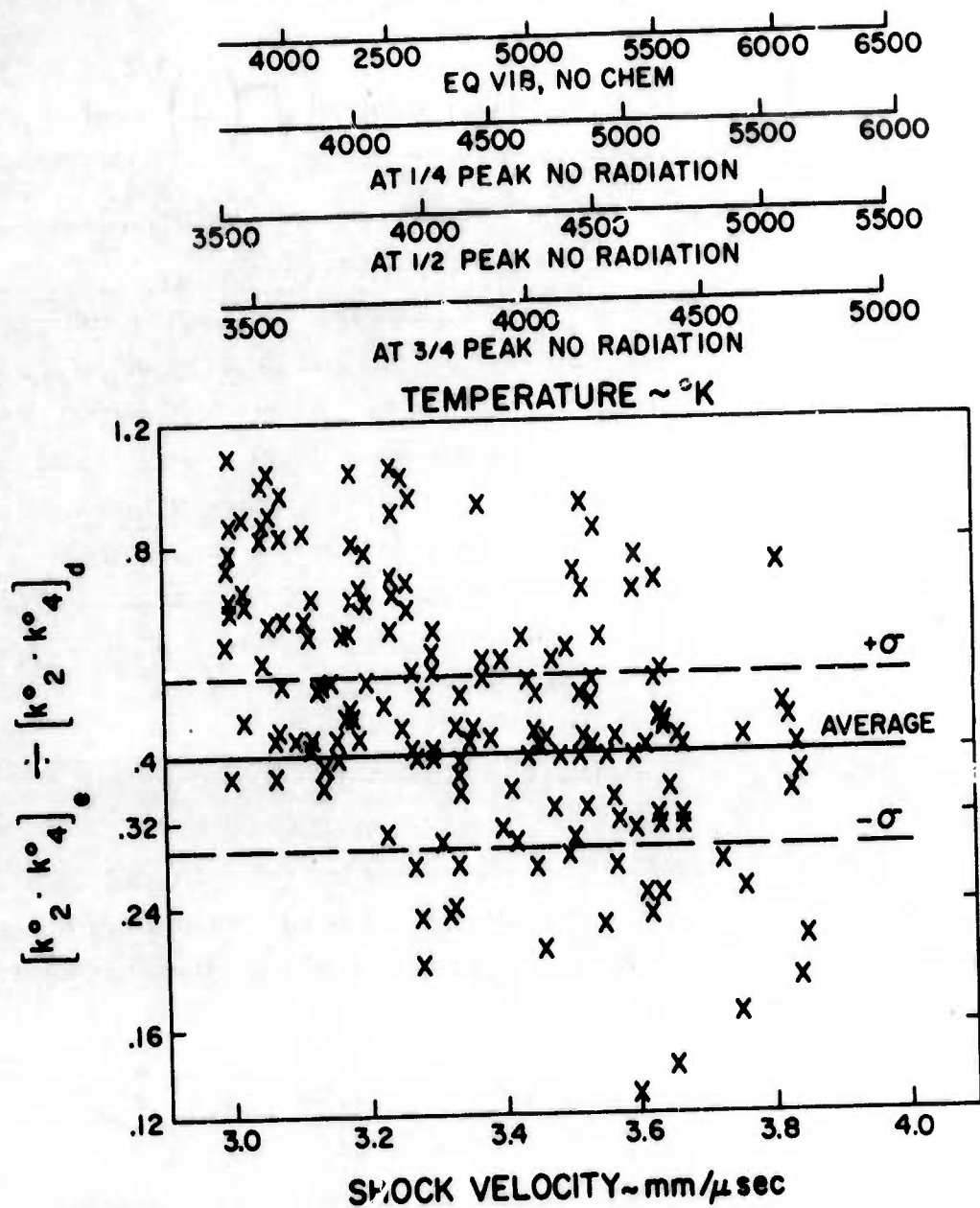


Fig. 23 The ratio of the experimental value of the rate constant product  $[k_2^o \cdot k_4^o]$  to that of Table I. The various gas temperatures are also shown.

from the computer calculations, at several NO emission levels. The solid line represents the average value and the dashed lines represent the standard deviation. A small number of the points shown in Fig. 23 were obtained from poor data and were given a larger uncertainty factor. The data seems to have a downward trend with increasing shock velocity, which can be fit with a  $T^2$  dependence. However, the scatter in the data and errors from fits to such a large exponential temperature dependence are too large to be certain of this trend. In addition, this downward trend could be due to shock wave attenuation effects, which would increase the rate constants at the lower shock speeds, where the event being measured occurred further from the shock front.

Our experimentally measured rate coefficient product,  $[k_2^0 k_4^0]$  is  $0.40 \pm 0.12$  of the rates given in Table I. This product involves four rate constant expressions. There is about a factor 2 uncertainty in the published rate constant expressions for  $k_{4,O_2}^{33}$ ,  $k_{4,O}^{33}$  and  $k_2^4$ . The value for  $k_{4,N_2}$  is an upper limit.<sup>3</sup> If  $k_{4,N_2}$  were dropped by a factor of 3, then the  $O_2$  dissociation by  $N_2$  would be negligible. The rate constant product above would decrease by a factor 2, producing essential agreement between the rate shown in Table I and our experimental results. A decrease of  $k_2$  or  $k_{4,O}$  by a factor of 2 would also bring the rate shown in Table I in agreement with our experimental measurements. The values of the individual rate constants cannot be obtained from our data and would require further measurements with various  $N_2$ - $O_2$  mixtures.

### Conclusion

We have reported on infrared measurements of NO formation in shock heated air from which the important reaction rate constants were evaluated. Our experimental value of the NO 5.3 micron fundamental band intensity is  $124 \pm 22 \text{ atm}^{-1} \text{ cm}^{-2}$ .

The reaction  $N_2 + O_2 \rightarrow 2NO$  proposed by Freedman and Daiber<sup>11</sup> and Wray and Teare<sup>9</sup> is incorrect. We obtained data repeating their experiment on shock heated NO to which they attributed the reverse of the above reaction. We have shown that the NO depletion was due mainly to  $2NO \rightarrow N_2O + O$ .

Without Reaction (1), NO production is initially slow until formation of atomic O, but then proceeds rapidly by the atom shuttle reactions. The NO production depends on the rate constant product,  $k_2 k_4$ .

It was shown that corrections due to the shock tube boundary layer growth must be included in order to obtain detailed agreement between experiment and calculations. The method is developed in Appendix C. An analysis of the vibrational relaxation of NO-O<sub>2</sub> mixtures is presented in Appendix A. NO vibration lag is small and does not affect the data analysis.



## APPENDIX A

### NO VIBRATION RELAXATION IN AIR

The theory of vibrational relaxation in a mixture of diatomic molecules is reviewed. Numerical estimates are then presented for the relaxation of an  $N_2$ - $O_2$ -NO mixture. Our specific problem is to determine the vibrational temperature history of a trace amount (less than  $10^{-2}$  concentration) of NO in temperatures ranging from  $2000^\circ K$  to  $6500^\circ K$ , corresponding to shock velocities from 2.0 to 4.0 mm per microsecond, see Fig. 1.

In a mixture of diatomic gases, the vibrational relaxation rate of each component can differ. This leads to added complexity in the number of ways in which to excite vibration. Not only is there the usual vibrational excitation in which collisional energy is converted to vibration, designated as a (TV) process, but vibrational energy can be transferred from one gas species to another, designated as a (VV) process. Consider the example of an  $N_2$ - $O_2$  mixture for which there are five vibrational excitation reactions.



The asterisk indicates vibrational excitation. The first four are (TV) processes; the last one a (VV) process.

In a mixture of the three molecules NO,  $N_2$  and  $O_2$ , there are 12 reaction paths: 3 pure gas (TV) processes, similar to Reaction (A-1); 3 (VV) processes, like Reaction (A-5); and 6 two-component (TV) processes like Reactions (A-3) and (A-4). Of these, 7 have been experimentally studied. Extensive measurements of the vibrational relaxation of  $O_2^{34,35}$ ,  $N_2^{29,36}$  and



NO<sup>37, 38</sup> have been reported. Vibrational relaxation in O<sub>2</sub>-N<sub>2</sub><sup>30, 36</sup> and NO-N<sub>2</sub><sup>31</sup> mixtures has been observed. The experimental relaxation times for these gases for a pressure of one atmosphere are plotted as a function of T<sup>-1/3</sup> in Fig. A-1 as the solid lines.

Estimates of the rate constants for the other reactions were obtained from theory. The dashed curves in Fig. A-1 give the vibrational relaxation times at one atmosphere pressure as a function of temperature. The measured NO-N<sub>2</sub><sup>31</sup> and O<sub>2</sub>-N<sub>2</sub><sup>30</sup> vibration exchange rates were 1/10 the theoretically predicted rate.<sup>39</sup> Thus, the O<sub>2</sub>-NO vibration exchange rate was also set at 1/10 the theoretical rate. The estimated (TV) reaction rates are not important reactions for relaxation in a trace NO-air mixture.

By combining the rate constants obtained from experimental measurements and theoretical predictions, we can estimate NO relaxation in air. We followed the mathematical treatment of Schwartz, Slawsky and Herzfeld<sup>39</sup> for vibrational relaxation in a mixture of diatomic molecules. Starting with Eq. (22) of Ref. 39, the rate of production of vibrational energy,  $E_a$ , in a mixture of three molecules designated by the subscripts a, b and c becomes\*

$$\begin{aligned} \frac{dE_a}{dt} = & \left[ \psi_a M_{aa} P_{aa} + \psi_b M_{ab} P_{ab} + \psi_c M_{ac} P_{ac} \right] (1 - e^{-h\nu_a/kT}) (E_a^* - E_a) + \\ & + \psi_b M_{ab} P_{ab}^e \left[ \frac{E_b}{E_b^*} \frac{1 - e^{-h\nu_a/kT}}{1 - e^{-h\nu_b/kT}} (E_a^* - E_a) - \left( 1 - \frac{E_b}{E_b^*} \right) E_a \right] + \\ & + \psi_c M_{ac} P_{ac}^e \left[ \frac{E_c}{E_c^*} \frac{1 - e^{-h\nu_a/kT}}{1 - e^{-h\nu_c/kT}} (E_a^* - E_a) - \left( 1 - \frac{E_c}{E_c^*} \right) E_a \right] \end{aligned} \quad (A-6)$$

$\psi_a$  is the mole fraction of the ath molecule. Thus,  $\psi_a + \psi_b + \psi_c = 1$ .  $E_a^*$  is the equilibrium vibrational energy at the translational temperature, T.

Since a harmonic oscillator potential was used in the derivation of Eq. (A-6),

\*Equation (22) of Ref. 39 has a few mistakes. Their previous Eq. (20) is correct and would give the formulation above for their Eq. (22).

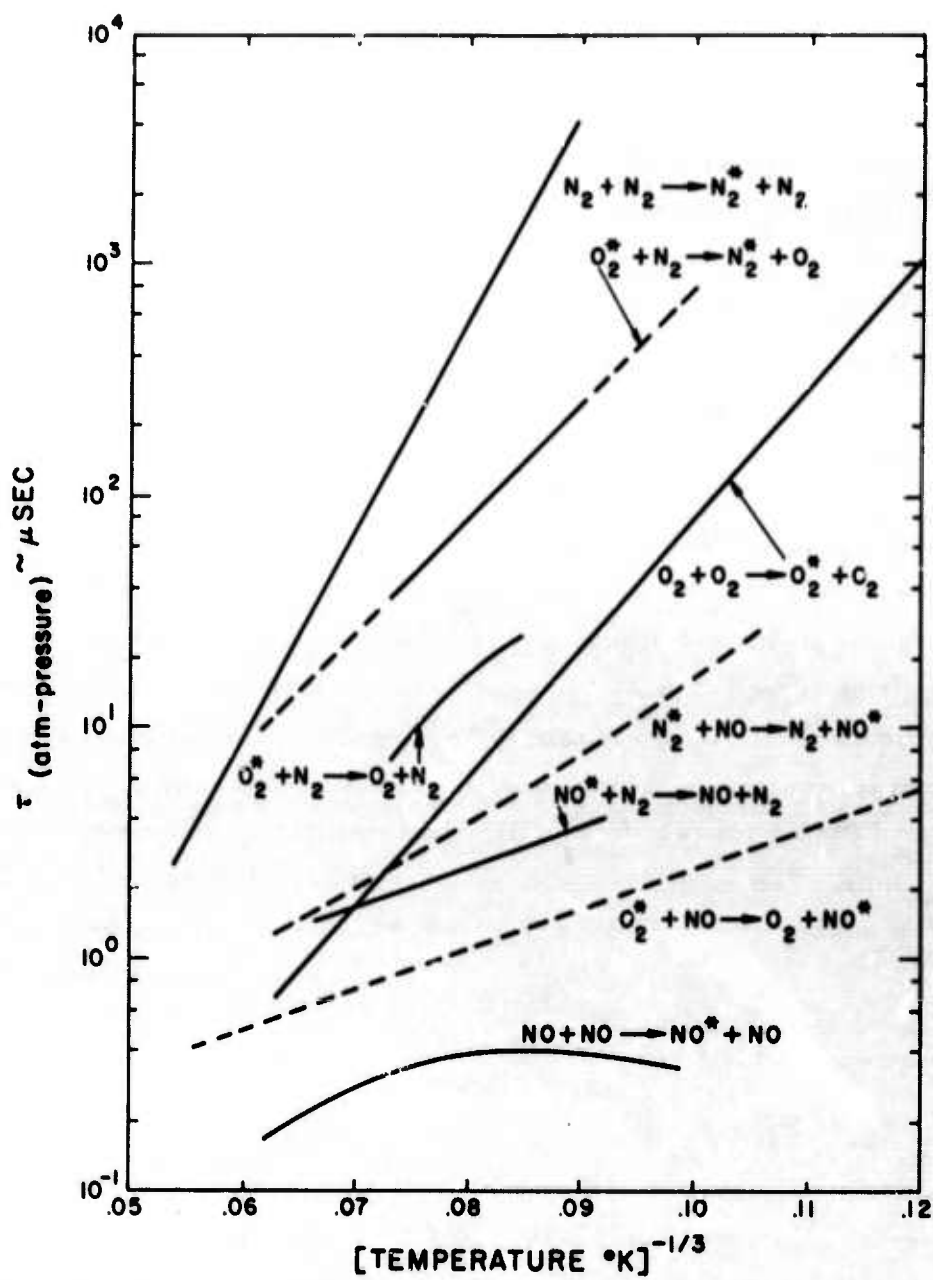


Fig. A-1 Vibration relaxation times as a function of shock velocity. Of the twelve possible reactions, only the important ones are shown.

$E_a^*$  has the simple form

$$E_a^* = \frac{\psi_a N h \nu_a}{e^{\frac{h \nu_a}{kT}} - 1} \quad (A-7)$$

$N$  is the total number of molecules per  $\text{cm}^3$ . The harmonic oscillator molecular potential has equally spaced vibrational levels with energy spacing ( $h\nu$ ).  $M_{ij}$  is the number of collisions per second that an  $i$ th molecule makes with  $j$ th molecules, assuming there are  $N$   $j$ th molecules per  $\text{cm}^3$ .  $M_{ij}$  is obtained from the relation

$$M_{ij} = N \bar{c} (R_i + R_j)^2 = N \sqrt{\frac{8kT}{m_i m_j}} (m_i + m_j) (R_i + R_j)^2. \quad (A-8)$$

$\bar{c}$  is the mean particle velocity based on the reduced mass of an  $i$  and  $j$  molecule;  $m$  and  $R$  are the mass and radius.  $P_{ij}$  is the probability that in a collision of an  $i$ th and  $j$ th molecule, the  $i$ th molecule makes the vibrational transition ( $v_i = 1$  to  $v_i = 0$ ) transferring energy to the translation mode.  $v_i$  is the vibrational quantum number.  $P_{ij}^e$  is the probability that in a collision of an  $i$ th and  $j$ th molecule, vibrational energy is exchanged in the transition ( $v_i = 1$  to  $v_i = 0$ ) and ( $v_j = 0$  to  $v_j = 1$ ). Differential equations for the relaxation of  $E_b$  and  $E_c$  are similar to Eq. (A-6) and are obtained by suitably changing the subscripts. There are two simplifications: from Eq. (A-8)

$$M_{ij} = M_{ji} \quad (A-9)$$

and theory predicts<sup>39</sup>

$$P_{ji}^e = P_{ij}^e e^{-h(\nu_i - \nu_j)/kT} \quad (A-10)$$

No general relation between  $P_{ij}$  and  $P_{ji}$  will be assumed. It can be shown<sup>17</sup> that a system with an harmonic oscillator potential and which satisfies the harmonic oscillator selection rules has a vibrational temperature  $T_v$  during the entire relaxation process, which is related to the vibrational energy

$$E_a = \frac{\psi_a N h \nu_a}{e^{\frac{h \nu_a}{kT_v}} - 1} \quad (A-11)$$

In order to relate the set of relaxation equations to the experimental measurements, we transform equations of the (A-6) type to those in terms of the vibrational relaxation times. For a (TV) process, the vibrational relaxation time  $\tau_{ij}$  is defined

$$1/\tau_{ij} = M_{ij} P_{ij} (1 - e^{-h\nu_i/kT}) . \quad (A-12)$$

For a (VV) process, the relaxation time  $\tau_{ij}^e$  is defined

$$1/\tau_{ij}^e = M_{ij} P_{ij}^e . \quad (A-13)$$

Comparing Eq. (A-13) with Eq. (A-10), we obtain

$$\tau_{ij}^e = \tau_{ji}^e e^{-h(\nu_i - \nu_j)/kT} = \tau_{ji}^e (\Theta_i / \Theta_j) , \quad (A-14)$$

where  $\Theta_i \equiv e^{-h\nu_i/kT}$ . We introduce the new dependent variable

$$X_i \equiv (E_i^* - E_i) / E_i^* , \quad (A-15)$$

which is preferable to the energy as it varies exponentially with time for systems with only (TV) processes.

Substituting Eqs. (A-12) through (A-15) into Eq. (A-6) and specifying a NO-N<sub>2</sub>-O<sub>2</sub> mixture, one obtains the relaxation equations

$$\begin{aligned} -\frac{dX_{O_2}}{dt} = & \left[ \frac{\psi_{O_2}}{\tau_{O_2-O_2}} + \frac{\psi_{N_2}}{\tau_{O_2-N_2}} + \frac{\psi_{NO}}{\tau_{O_2-NO}} \right] X_{O_2} - \frac{\psi_{N_2}}{\tau_{O_2-N_2}^e} \left[ \frac{X_{N_2}(1-X_{O_2})}{1-\Theta_{O_2}} - \frac{X_{O_2}(1-X_{N_2})}{1-\Theta_{N_2}} \right] \\ & (1-\Theta_{O_2}) - \frac{\psi_{NO}}{\tau_{O_2-NO}^e} \left[ \frac{X_{NO}(1-X_{O_2})}{1-\Theta_{O_2}} - \frac{X_{O_2}(1-X_{NO})}{1-\Theta_{NO}} \right] (1-\Theta_{O_2}) \end{aligned} \quad (A-16a)$$

$$-\frac{dX_{N_2}}{dt} = \left[ \frac{\psi_{O_2}}{\tau_{N_2-O_2}} + \frac{\psi_{N_2}}{\tau_{N_2-N_2}} + \frac{\psi_{NO}}{\tau_{N_2-NO}} \right] + \frac{\psi_{O_2}(\theta_{O_2}/\theta_{N_2})}{\tau_{O_2-N_2}^e} \left[ \frac{X_{N_2}(1-X_{O_2})}{1-\theta_{O_2}} - \frac{X_{O_2}(1-X_{N_2})}{1-\theta_{N_2}} \right] (1-\theta_{N_2}) + \quad (A-16b)$$

$$+ \frac{\psi_{NO}(\theta_{NO}/\theta_{N_2})}{\tau_{NO-N_2}^e} \left[ \frac{X_{N_2}(1-X_{NO})}{1-\theta_{NO}} - \frac{X_{NO}(1-X_{N_2})}{1-\theta_{N_2}} \right] (1-\theta_{N_2})$$

$$-\frac{dX_{NO}}{dt} = \left[ \frac{\psi_{O_2}}{\tau_{NO-O_2}} + \frac{\psi_{N_2}}{\tau_{NO-N_2}} + \frac{\psi_{NO}}{\tau_{NO-NO}} \right] + \frac{\psi_{O_2}(\theta_{O_2}/\theta_{NO})}{\tau_{O_2-NO}^e} \left[ \frac{X_{NO}(1-X_{O_2})}{1-\theta_{O_2}} - \frac{X_{O_2}(1-X_{NO})}{1-\theta_{NO}} \right] \cdot \quad (A-16c)$$

$$\cdot (1-\theta_{NO}) - \frac{\psi_{N_2}}{\tau_{NO-N_2}^e} \left[ \frac{X_{N_2}(1-X_{NO})}{1-\theta_{NO}} - \frac{X_{NO}(1-X_{N_2})}{1-\theta_{N_2}} \right] (1-\theta_{NO}) .$$

In order to obtain numerical solutions, each  $\tau$  and  $\theta$  must be specified. Numerical values for  $\tau$  may be obtained from Fig. A-1. Using published<sup>15</sup> molecular constants,

$$\theta_{O_2} = e^{-2239^\circ K/T}; \theta_{NO} = e^{-2702^\circ K/T}; \theta_{N_2} = e^{-3353^\circ K/T} . \quad (A-17)$$

We obtain solutions of Eq. (A-16) for the specific case

$$\psi_{O_2} = 0.21; \psi_{N_2} = 0.79; \psi_{NO} = .0001 . \quad (A-18)$$

Equation (A-16) can be solved once the kinetic temperature is given as a function of time. For the shock tube experiments, the temperature  $T$  is obtained by combining Eq. (A-16) with the Rankine-Hugoniot relations across the shock for the conservation of mass, momentum and energy.



$$\begin{aligned}
 \rho u &= \rho_1 u_1 \\
 p + \rho u^2 &= p_1 + \rho_1 u_1^2 \\
 h + \frac{1}{2} u^2 &= h_1 + \frac{1}{2} u_1^2
 \end{aligned}
 \tag{A-19}$$

For our experimental conditions, the perfect gas relation applies

$$p = \rho RT, \tag{A-20}$$

and the enthalpy per unit weight  $h$  is given by

$$h = 3.5RT + \frac{1}{\rho} (E_{O_2} + E_{N_2} + E_{NO}). \tag{A-21}$$

The vibrational energies are obtained from solutions of Eq. (A-16).

The set of equations (A-16, 19, 20 and 21) was programmed for a 7090 computer. Figure A-2 shows the behavior of  $X_{NO}$ ,  $X_{O_2}$  and  $X_{N_2}$  with time, for a shock velocity of 2.0 mm per microsecond, 5 torr initial pressure, 297°K initial temperature, and 0.01% NO in air.

There are several important features to these curves: (1) initially, the  $O_2$ , NO and  $N_2$  relax without (VV) processes; (2) (VV) processes become important after sufficient  $O_2$  excitation; and (3) finally, the three gases follow a single relaxation time. The NO quickly relaxes to about 60% of equilibrium and then follows the final relaxation rate.  $\tau_{NO-O_2}^e$  being uncertain was changed by a factor of 3 and 0.3; this has only a small effect on the NO relaxation. Figures A-3 and A-4 show the  $X_{NO}$ ,  $X_{O_2}$  and  $X_{N_2}$  variation with time for shock velocities of 2.5 and 3.0 mm per microsecond using the same initial conditions. These calculations of the NO vibrational relaxation time in shock heated air are used to determine the decrease in the infrared emission due to vibration lag. The infrared emission is proportional to the vibrational energy, see Eq. (4). Thus, the ratio of the emission to that at equilibrium vibration is

$$I/I_{eq} = E/E^* = 1 - X_{NO}. \tag{A-22}$$

Values of  $I/I_{eq}$  presented in Fig. 11 were obtained from Figs. A-2, A-3 and A-4, using Eq. (A-22).



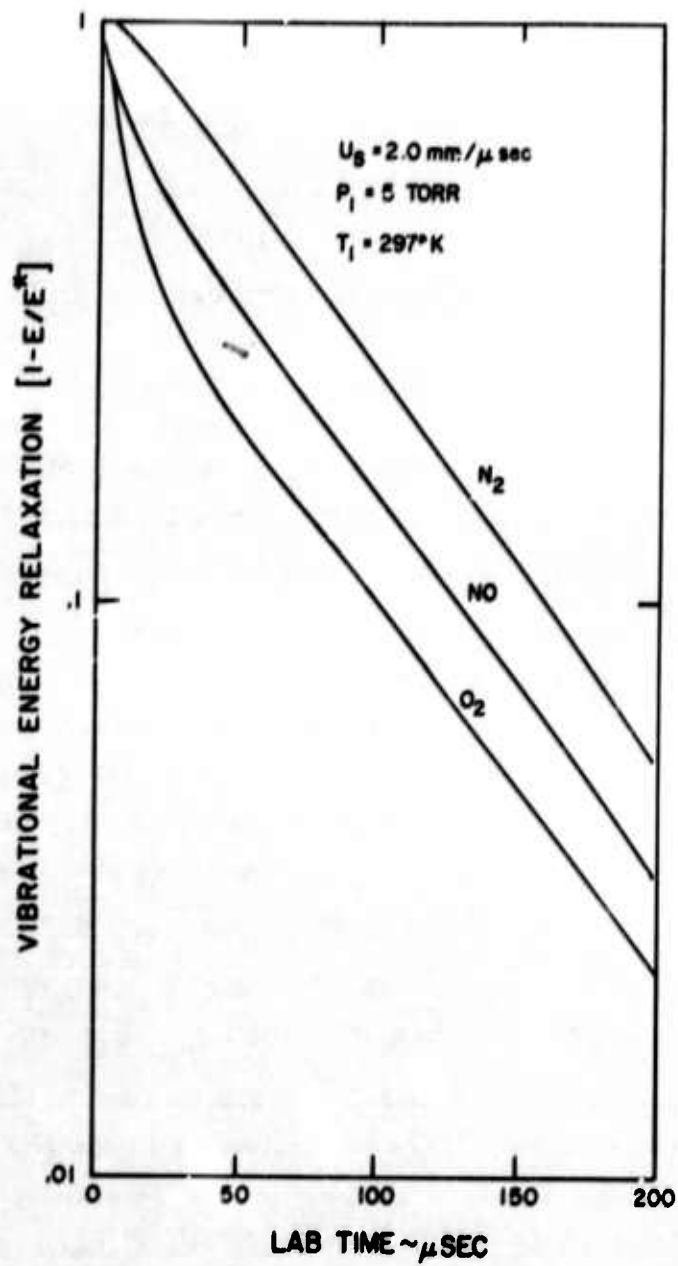


Fig. A-2 The fraction of energy in vibration as a function of time.

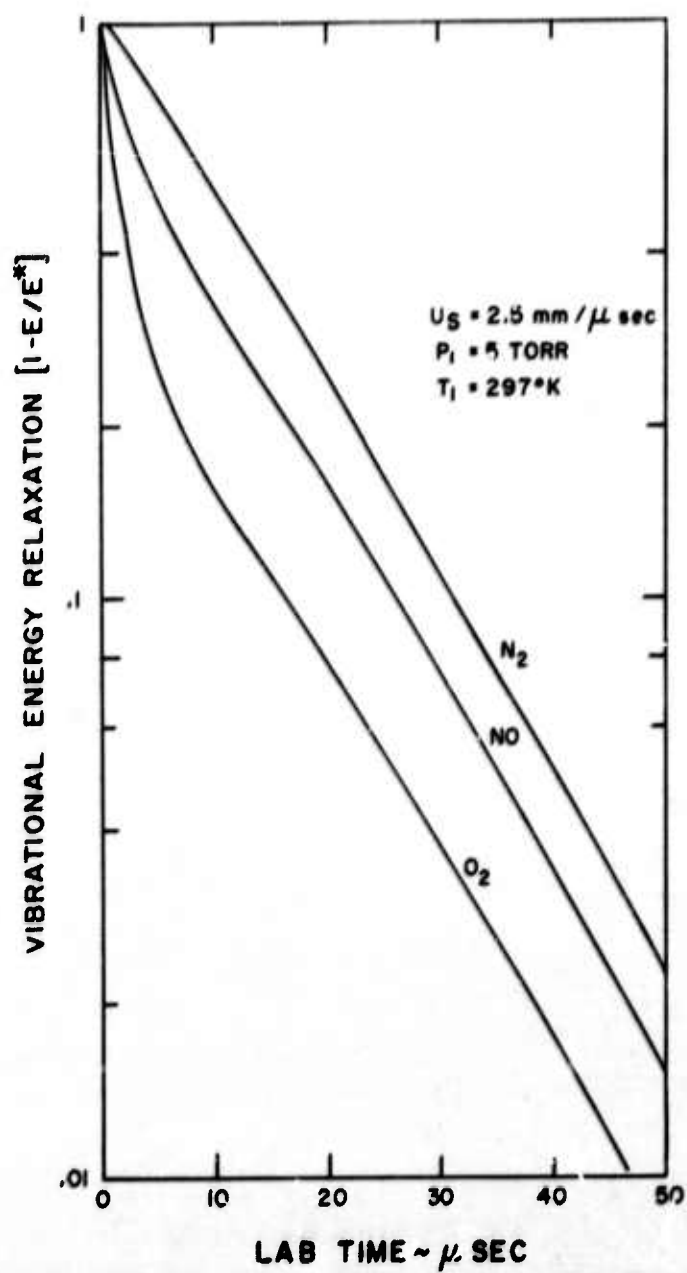


Fig. A-3 The fraction of energy in vibration as a function of time.

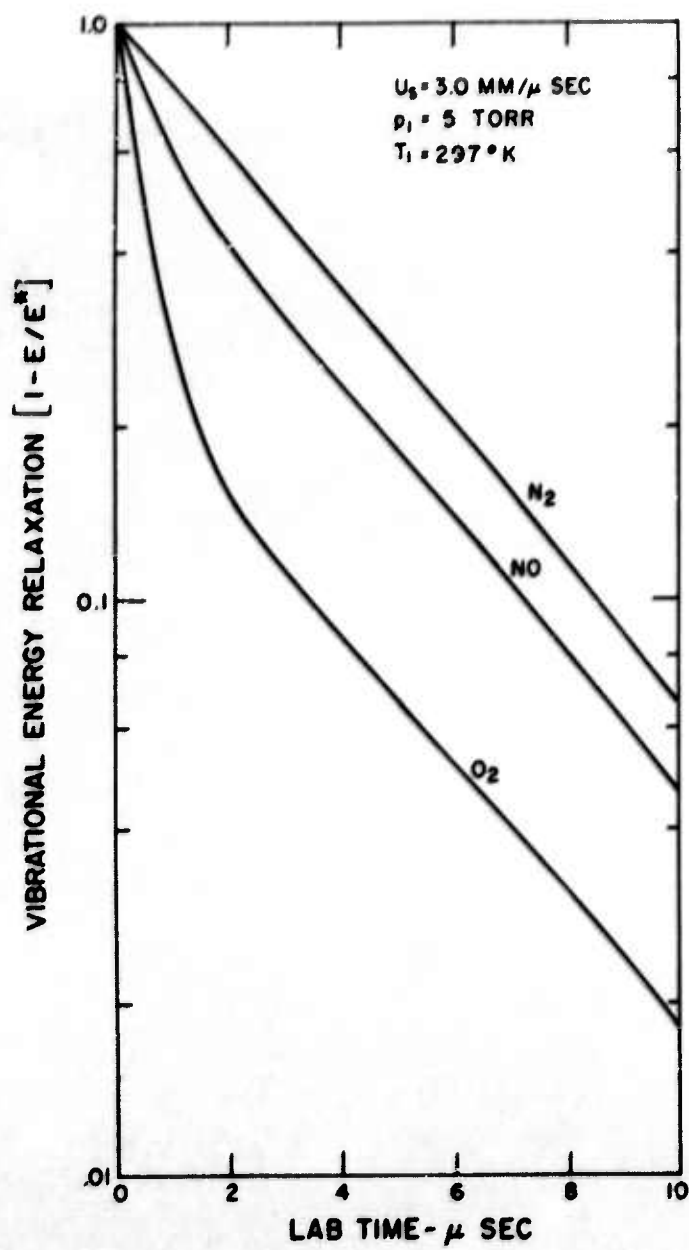


Fig. A-4 The fraction of energy in vibration as a function of time.

## APPENDIX B

### CALIBRATION OF INFRARED SYSTEM

There are two parts to this appendix. First, the mathematics is developed for calibrating the infrared system. These formulas are used in Section III to determine the NO fundamental band strength. Second, we show that the weak line approximation is valid for the analysis of the shock tube data.

The infrared system calibration is determined from the molecular constants for the 5.3 micron NO fundamental vibration-rotation band. In the general case, the radiation depends upon the gas composition, temperature, optical path, and density. See, for example, the treatments of Breen,<sup>40</sup> and Carpenter and Franzosa.<sup>41</sup> In this experiment, the NO concentrations and partial pressures are low enough so that the effects of self-absorption are not important. We shall show at the end of this appendix that the gas is optically thin; thus, the intensity is simply the sum of the emission from each molecule.

The notation of Herzberg<sup>15</sup> is used. The NO ground electronic state is a  $^2\Pi_{3/2, 1/2}$  doublet system with three branches of two closely spaced lines. For our purposes, this system can be approximated with the formulas for the symmetric top with  $\Lambda = 1$ . The emission lines in the three branches of the fundamental band are produced by the vibrational transitions  $v'$  to  $v'' = (v' - 1)$  and the rotation transitions

$$\text{P branch: } J' \text{ to } J'' = J' + 1 \qquad J' = 1, 2, 3, \dots \qquad (\text{B-1a})$$

$$\text{Q branch: } J' \text{ to } J'' = J' \qquad J' = 1, 2, 3, \dots \qquad (\text{B-1b})$$

$$\text{R branch: } J' \text{ to } J'' = J' - 1 \qquad J' = 2, 3, 4, \dots \qquad (\text{B-1c})$$

$v$  and  $J$  are the quantum numbers for the vibration and rotation levels, respectively. The prime and double prime superscripts correspond to the upper and lower states in the transition. The wave numbers of the rotation lines for the P, Q and R branches are

$$\nu_P = \nu_{v'} - 2(J'+1)B_e - a_e [(J'+1)^2 - 2(J'+1)v' - 1] \quad J' = 1, 2, 3, \dots \quad (B-2a)$$

$$\nu_Q = \nu_{v'} - a_e (J'^2 + J' - 1) \quad J' = 1, 2, 3, \dots \quad (B-2b)$$

$$\nu_R = \nu_{v'} + 2J' B_e - a_e [J'^2 + 2J'v' - 1] \quad J' = 2, 3, 4, \dots \quad (B-2c)$$

The subscripts P, Q and R indicate the branches. At the band center the wave number  $\nu_{v'}$  with upper level  $v'$  is

$$\nu_{v'} = \omega_e - 2v' \omega_e x_e + 3.25 v'^2 \omega_e y_e = [1904.03 - 27.9 v' - 0.0039 v'^2] \text{ cm}^{-1} \quad (B-3)$$

$B_e$  and  $a_e$  are parameters pertaining to the rotation constants. For NO,  $B_e = 1.7046 \text{ cm}^{-1}$  and  $a_e = 0.0178 \text{ cm}^{-1}$ . Note that the P and R branches form a progression of almost equally spaced lines, except for three missing lines at the center: the  $J' = 0$  line in the P branch and the  $J' = 0$  and 1 lines in the R branch. The Q branch with closely spaced lines is at the center of the band. There is an R branch band head for each value of  $v'$ . For  $v' = 1$ , the band head occurs at  $2022 \text{ cm}^{-1}$  for  $J' = 84$ . The P branch does not have a band head and expands to smaller wave numbers.

The intensities of the rotation lines are

$$I_P = \frac{c_{em} \nu_P^4}{Q_v Q_r} \left( \frac{J'^2 + 2J'}{J' + 1} \right) e^{-hc [J'^2 + J' - 1] [B_e - a_e (v' + \frac{1}{2})] / kT} e^{-hc G_{v'} / kT} \quad (B-4a)$$

$$I_Q = \frac{c_{em} \nu_Q^4}{Q_v Q_r} \left( \frac{2J' + 1}{J'(J' + 1)} \right) e^{-hc [J'^2 + J' - 1] [B_e - a_e (v' + \frac{1}{2})] / kT} e^{-hc G_{v'} / kT} \quad (B-4b)$$

$$I_R = \frac{c_{em} \nu_R^4}{Q_v Q_r} \left( \frac{J'^2 - 1}{J'} \right) e^{-hc [J'^2 + J' - 1] [B_e - a_e (v' + \frac{1}{2})] / kT} e^{-hc G_{v'} / kT} \quad (B-4c)$$

$G_v$  is the term difference (in wave numbers) between the  $v^{\text{th}}$  vibration level and the ground level,  $v = 0$ ,

$$G_v = v[\omega_e - (v + 1) \omega_e x_e + (v^2 + 1.5 v + 0.75) \omega_e y_e] \quad (B-5)$$

Note  $G_{v=1} = \nu_1$ , compare Eq. (B-3) and (B-5).  $Q_v$  and  $Q_r$  are the partition functions for vibration and rotation.  $Q_r$  is a sum over the P, Q and R branches of the factors which contain  $J'$ .

$$Q_r = \sum_{J'=1}^{\infty} \left[ \frac{J'^2 + 2J'}{J'+1} + \frac{2J'+1}{J'(J'+1)} + \frac{J'^2-1}{J'} \right] e^{-hc [J'^2 + J' - 1] [B_e - a_e(v' + \frac{1}{2})]/kT}$$

$$\approx \frac{kT}{hc [B_e - a_e(v' + \frac{1}{2})]} \quad (B-6)$$

$Q_v$  is defined

$$Q_v = \sum_{v=0}^s e^{-hcG_v/kT} \approx (1 - e^{-hc\nu_1/kT})^{-1} \quad (B-7)$$

Breen<sup>40</sup> computed the matrix elements for the anharmonic potential of NO and finds that  $c_{em}$  is not constant but has a slight variation with  $v'$ . His result, for the fundamental band, changes  $c_{em}$  in Eq. (B-4) to

$$c_{em}^* (\nu_{v'=1}/\nu_{v'})^2 = c_{em}^* / [1 - 0.015(v'-1)]^2 \quad (B-8)$$

where  $c_{em}^*$  is the value of  $c_{em}$  for  $v'=1$ . This corrected matrix element was not used in our calculation as it has a negligible effect. At a temperature of 6000°K, it would increase the total emission by about 9%. At lower temperatures, the increase is even smaller.

Except for  $c_{em}$ , numerical values of all the quantities in Eq. (B-4) are now specified. Our experimental data will be used to determine  $c_{em}$ . We will use the following procedure.

In this experiment, we used broad band infrared (InSb and Ge: Au) detectors with interference filters to isolate the NO band, (see Fig. 5). Let  $\tau(\nu)$  be the transmission of the filter, and  $\sigma(\nu)$  the response of the detector; both quantities are functions of wave number  $\nu$ . The signal  $S$  observed by the detector is determined by the emission of the gas folded into the response of the detector and the filter transmission:

$$S = \ell \Omega \sum_{v'=1} \sum_{J'=1} [\sigma \tau I_P + \sigma \tau I_Q + \sigma \tau I_R] \quad (B-9)$$

$\Omega$  is the solid angle of the gas as seen by the detector. Inserting the values of  $I_P$ ,  $I_Q$  and  $I_R$  from Eq. (B-4) into (B-9), one obtains



$$S = \Omega_o X_o N l c_{em} \left\{ \sum_{v'=1} \sum_{J'=1} \frac{\sigma \tau \nu^{J'}}{\Omega_o \Omega_v} \left[ \frac{\nu_Q^{4(2J'+1)+\nu_P^{4J'^2(J'+2)+\nu_R^{4(J'+1)^2(J'-1)}}}{(J'+1)J'} \right] \right. \\ \left. - \frac{hc [J'^2 + J' - 1] [G_{v'} + B_e - a_e (v' + \frac{1}{2})]}{kT} \right\} \quad (B-10).$$

$\Omega_o$  is the solid angle of the optical system using the full 8-inch diameter mirror.  $X_o$  is the fraction of the mirror uncovered; that is,  $\Omega = \Omega_o X_o$  is the solid angle actually used.  $N$  is the NO number density, and  $l = 3.81$  cm is the diameter of the shock tube. The temperature dependence of the calibration shown in Fig. 7 was computed from the bracketed portion of Eq. (B-10); the height of the curve was adjusted for the best fit to the data. The dependence of  $\sigma$  and  $\tau$  on wave number is presented in Fig. 5.

The infrared system was also calibrated with a black body source at  $500^\circ\text{C}$ , for which the observed signal  $S_B$  was

$$S_B = X \Omega_o \int_0^\infty \sigma \tau I_B d\nu. \quad (B-11)$$

$I_B$  is the black body emission.  $X$  was a variable calibrated attenuator (aperture stop over mirror) that was adjusted to obtain the same signal range as observed in the shock tube runs. Combining the black body calibration data with the measured NO emission, one can determine the emission constant,  $c_{em}$ . Eliminating  $\Omega_o$  between Eqs. (B-10) and (B-11),  $c_{em}$  becomes

$$c_{em} = \left( \frac{N_o}{N l} \right) \left( \frac{S}{S_B} \right) \left( \frac{X}{X_o} \right) \frac{\int_0^\infty \sigma \tau I_B d\nu}{\left\{ \sum_{v'} \sum_{J'} \dots \right\}} \quad (B-12)$$

The brackets indicate the same summation given in Eq. (B-10). By using the ratio of the signals  $S$  to  $S_B$ , the calibration becomes independent of the solid angle  $\Omega_o$ , and dependent on only the spectral variation but not the absolute magnitude of  $\sigma$  and  $\tau$ . The function  $\int \sigma \tau I_B d\nu \left\{ \sum_{v'} \sum_{J'} \dots \right\}$  is

shown as a function of the NO temperature in Fig. B-1. A numerical value for  $c_{em}$  is determined from the experimental data in Section III with the use of Eq. (B-12).

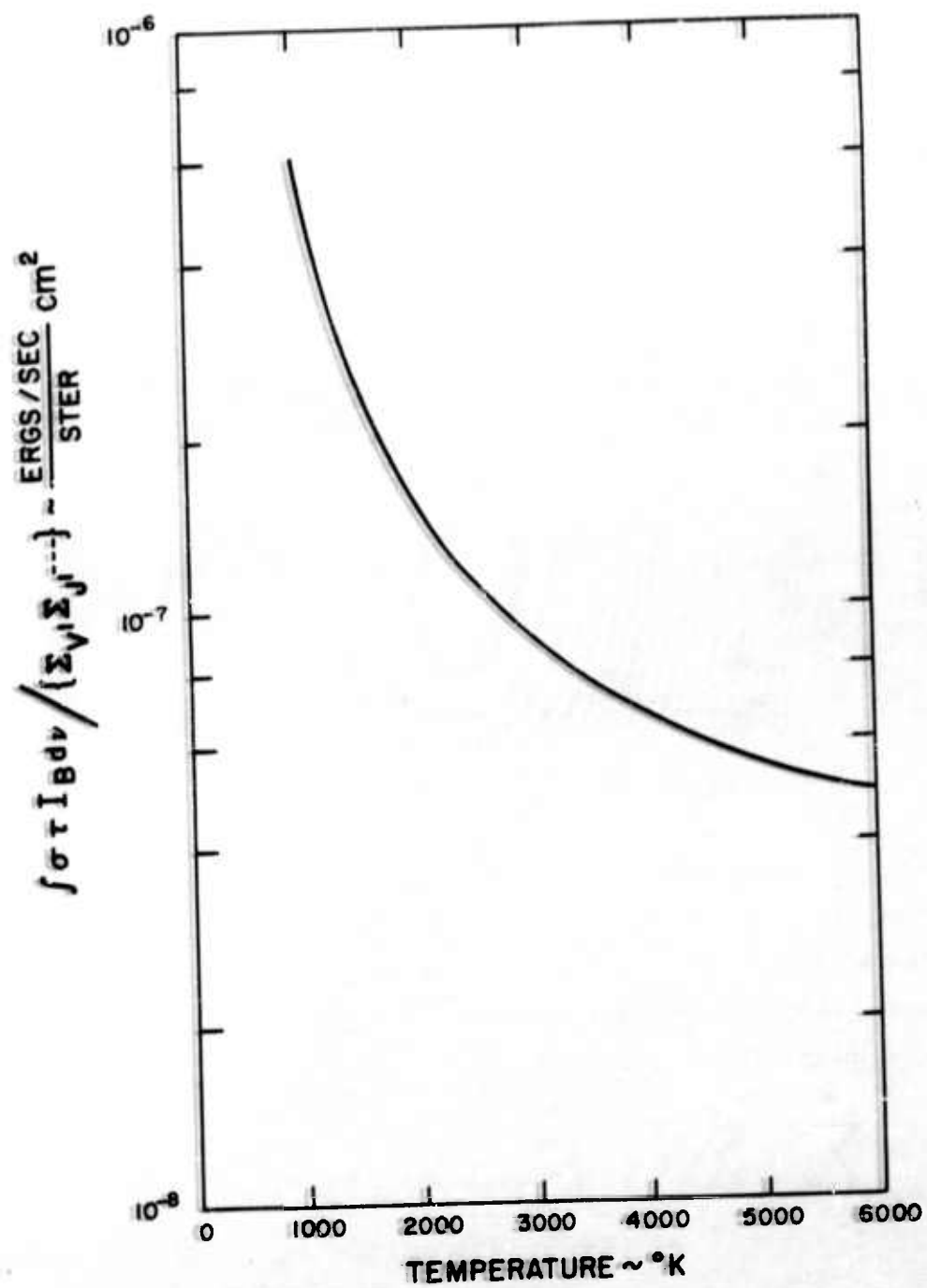


Fig. B-1 The black body function divided by the sum of the contributions of the individual lines as a function of NO temperature.

### Validity of Weak Line Approximation

We will prove that the gas is optically thin over our experimental conditions by showing that the gas emissivity at the center of each spectral line is much less than unity. The emissivity,  $\epsilon$ , of a layer of radiating gas can be written

$$\epsilon = 1 - \exp(-a N \mu)(1 - \exp[-hc\nu/kT]) \quad (B-13)$$

$\mu$  is the absorption coefficient per particle and  $N$  is the thickness of the gas sample in particles per  $\text{cm}^2$ ;  $a$  is a geometric coefficient of the order of 1. The factor  $(1 - \exp hc\nu/kT)$  varies between .4 and .9 for our experimental conditions. For  $\epsilon \ll 1$ , Eq. (B-13) reduces to

$$\epsilon \approx N \mu \quad (B-14)$$

Within the accuracy of this derivation, the factor  $a(1 - \exp[hc\nu/kT])$  is the order of unity and has been dropped. The emissivity for the absorbing state ( $v''$ ,  $J''$ ) is

$$\epsilon = N \mu_{(v'', J'')} = \frac{1}{2} \ell \psi P(v''+1)(273^\circ\text{K}/T) C_{\text{abs}} b_o \nu_R \left[ \left( \frac{J''^2 + 2J''}{J''+1} \right) \frac{-(G_{v''} + [B_e - a_e(v'' + \frac{1}{2})][J''^2 + J'' - 1])hc\nu/kT}{Q_r Q_v} \right] \quad (B-15)$$

The factor  $\frac{1}{2}$  is due to the doublet system. An R branch line is used as it has the maximum absorption.  $P$  is the pressure;  $\psi P$  is the partial pressure of NO;  $b_o$  is the line width factor.  $C_{\text{abs}}$  is determined from the measured integral absorption over the band.

$$\sum_{v''=0}^{\infty} \sum_{J=1}^{\infty} \int_{\text{band}} \mu_{v'', J''} d\nu \approx C_{\text{abs}} \nu_1 = 124 \text{ atm}^{-1} \text{ cm}^{-2} \quad (B-16)$$

$P, Q, R$

Using  $\nu_1 = 1876 \text{ cm}^{-1}$ , the band center wave number,  $C_{\text{abs}}$  becomes

$$C_{\text{abs}} = \frac{124}{(1876)} = 0.066 \text{ atm}^{-1} \text{ cm}^{-1} \quad (B-17)$$

Let  $b(\nu)$  be the spectral shape of the line. In the general case, where there is both collision and Doppler broadening, the line shape becomes

$$b(\nu) = \frac{\sqrt{\ell n 2}}{\pi^{3/2}} \left(\frac{a}{\beta}\right) \int_{-\infty}^{\infty} \frac{\exp [-(4 \ell n 2)(\nu' - \nu_R)^2 / \beta^2]}{(a/2)^2 + (\nu - \nu')^2} d\nu' \quad (\text{B-18})$$

$a$  and  $\beta$  are the full widths of the line at half amplitude for collision and Doppler broadening, respectively. Equation (B-18) is normalized for each line so that  $b(\nu) d\nu = 1$ . At the center of the line, say  $b_0$ , where the absorption is maximum, Eq. (B-18) becomes<sup>42</sup>

$$b_0 \equiv b(\nu = \nu_R) = \sqrt{\frac{\ell n 2}{\pi}} \left(\frac{1}{\beta}\right) \exp\left[\left(\frac{a}{\beta}\right) (\ell n 2)\right] \operatorname{erfc}\left[\frac{a}{\beta} \sqrt{\ell n 2}\right] \quad (\text{B-19})$$

The collision broadened line width at standard temperature and density,  $a_0$ , was measured for collisions with Ar;  $a_0 = 0.06 \text{ cm}^{-1}$ . We assume the same value of  $a_0$  for collisions with  $\text{O}_2$  and  $\text{N}_2$ . The dependence of  $a$  on temperature and total pressure is

$$a = \frac{P}{P_0} a_0 \sqrt{\frac{T_0}{T}} \quad (\text{B-20})$$

where  $T_0 = 273^\circ\text{K}$  and  $P_0 = 1$  atmosphere pressure. The Doppler half width is

$$\beta = (.0040 \text{ cm}^{-1}) (\nu_R/\nu_1) \sqrt{T/T_0} \quad (\text{B-21})$$

For our experimental conditions, the line width is less than  $0.025 \text{ cm}^{-1}$ . This should be compared to the average spacing between lines of  $3.4 \text{ cm}^{-1}$ . Thus, the spacing is 100 times the line widths; the overlap of lines is negligible. Also negligible is the overlapping of lines of the P and R progressions for different vibration levels,  $\nu''$ .

By optimizing Eq. (B-15), one can show that the  $\epsilon$  has the maximum value for the R branch line with  $\nu'' = 0$  and  $J'' = Q_r/2$ . Using these values of  $J''$  and  $\nu''$ , and combining Eqs. (B-16) and (B-15), one obtains the desired form for the maximum emissivity.

$$\epsilon = 62 \ell b_0 \left(\frac{P\Psi}{P_0}\right) \left(\frac{T_0}{T}\right) \left(\frac{hc B_e}{kT}\right)^{1/2} \frac{1}{\sqrt{2e}} (1 - e^{-hc\nu_1/kT}) \quad (\text{B-22})$$

When evaluating Eqs. (B-19) and (B-22) over the experimental conditions shown in Figs. 1, 2 and 3, it is found that  $\epsilon < 0.1$ . Thus, the gas is optically thin at the center of each line.



## APPENDIX C

### EFFECTS OF BOUNDARY LAYER GROWTH ON SHOCK TUBE WALLS

Many investigations of boundary layer growth on shock tube walls have been reported. These have mainly been concerned with the effect of the boundary layer on shock tube test times and on the variation of equilibrium conditions along the shock tube axis caused by the boundary layer growth. Mirels<sup>43</sup> discussed these effects in terms of a "limiting separation distance," first observed by Duff.<sup>44</sup> This concept is depicted in Fig. C-1, taken from Ref. 43. A normal shock wave with velocity  $U_s$  is advancing into stationary gas; the profiles in the figure show velocities relative to the shock front, and in this coordinate system the shock tube walls are moving with the shock velocity. Ahead of the shock the relative velocity of the gas is supersonic, while immediately behind the shock the velocity,  $u_{eo}$ , is given by  $\rho_{eo} u_{eo} = \rho_1 U_s$ . As the boundary layer develops,  $u_e$  and  $\rho_e$  change, such that the integral of  $\rho u$  over the entire shock tube area is conserved. However, in this coordinate system the boundary layer is a region in which  $\rho > \rho_e$  and  $u > u_e$ , corresponding to a negative displacement thickness. Thus the gas which has not yet entered the boundary layer behaves as if it were in a divergent channel, resulting in a decrease of  $u_e$  with increasing distance behind the shock, since  $u_{eo}$  is necessarily subsonic. Ultimately the boundary layer grows such that the integral of  $\rho u$  across the boundary layer area is equal to the integral of  $\rho_{eo} u_{eo}$  across the entire tube area. At this point, a distance  $x_\ell$  behind the shock wave, the central test gas is stagnated.

In terms of the operation of a shock tube, the phenomena may be described as follows: after rupture of the diaphragm and establishment of a plane shock wave, the distance between the shock and the contact surface initially grows with time. Once this distance has reached the limiting separation distance  $x_\ell$ , the rate of flow of cold gas through the shock wave is exactly balanced by the rate of outflow through the boundary layer at  $x = x_\ell$ , and no further increase of length of the "test slug" occurs. When a shock tube of conventional length is operated at sufficiently high



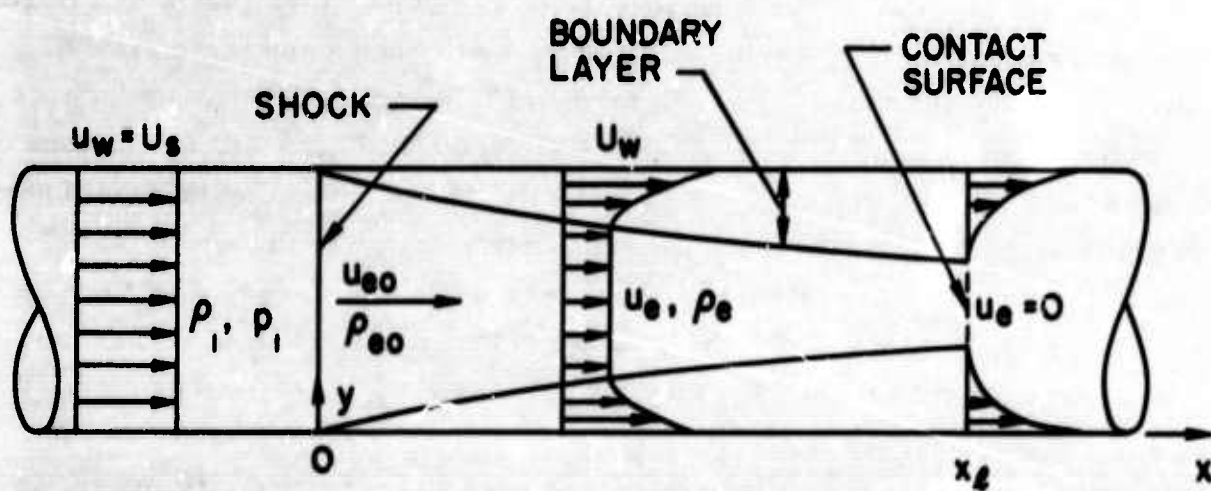


Fig. C-1 A schematic representation of the quantities used in calculating the effects of the side wall boundary layer.

pressure this maximum length of test slug is not achieved, and the variation of  $u_e$  with distance behind the shock may be negligible during the experimental test time. However, for many chemical kinetics experiments the shock tube initial pressure must be kept low in order to obtain a finite relaxation zone. Under such conditions the experimental observations may continue over almost the entire available test time, and significant errors may then be incurred in the data analysis if the variation of  $u_e$  is neglected.

The variation of  $u_e$  has a two-fold effect on the interpretation of shock tube kinetics data. In the first place the deceleration of the subsonic flow relative to the shock wave increases the static enthalpy of the test gas, and this can have a marked effect on the reaction rates of reactions with steep temperature dependence. Secondly, the deceleration results in increased flow time for a given gas sample as it flows from the shock wave to the point of observation. The distance from the shock to the point of observation is

$$x = \int u_e dt_P ,$$

where  $t_P$  is the particle time measured from the shock front. In the laboratory coordinate system, the time  $t_L$  is measured from the arrival of the shock at the observation station, so that

$$t_L = x/U_s = \int (u_e/U_s) dt_P .$$

In the absence of boundary layer effects, the ratio  $u_e/U_s = \rho_1/\rho_e$ , and is affected only by changes in  $\rho_e$  as chemical reactions proceed, but when  $u_e$  can decrease towards zero it is clear that  $dt_P/dt_L$  can become very large as  $x$  approaches the value  $x_f$ .

In the present study of NO formation in shock heated air it was apparent that some of the data obtained at low initial pressures were affected by the boundary layer growth. In comparing the data with theoretical calculations, it was thus necessary to include the effective area variation of the channel in which the reacting gas flows after passage through the shock wave. In the conventional constant area 1-dimensional

normal shock chemistry calculation it is usual<sup>9</sup> to integrate the various chemical rate equations subject to constraints imposed by the shock conservation equations, which can be written in the form

$$p_e = p_1 + \rho_1 U_s^2 (1 - \rho_1 / \rho_e)$$

$$\text{and } h_e = h_1 + \frac{1}{2} U_s^2 \left\{ 1 - (\rho_1 / \rho_e)^2 \right\}$$

since  $\rho_e u_e = \rho_1 U_s$ .

In the present case, it was more expedient to modify a stream-tube program<sup>45</sup> to permit integration of the chemical rate equations subject to constraints imposed by a specified variation of area with distance.

Thus the governing equations become

$$h_e + \frac{1}{2} u_e^2 = h_1 + \frac{1}{2} U_s^2 \quad (C-1)$$

$$\rho_e u_e A = \rho_1 U_s A_0 \quad (C-2)$$

$$\text{and } \frac{dp_e}{dt_P} = -\rho_e u_e \frac{du_e}{dt_P}, \quad (C-3)$$

$$\text{with } p_e = z_e \rho_e R T_e \quad (C-4)$$

Equations C-1, C-2 and C-4 can be written in the form

$$\frac{dh_e}{dt_P} = -u_e \frac{du_e}{dt_P} \quad (C-5)$$

$$\frac{1}{\rho_e} \frac{d\rho_e}{dt_P} + \frac{1}{u_e} \frac{du_e}{dt_P} + \frac{1}{A} \frac{dA}{dt_P} = 0 \quad (C-6)$$

$$\text{and } \frac{1}{p_e} \frac{dp_e}{dt_P} = \frac{1}{z_e} \frac{dz_e}{dt_P} + \frac{1}{\rho_e} \frac{d\rho_e}{dt_P} + \frac{1}{T_e} \frac{dT_e}{dt_P}. \quad (C-7)$$

Eliminating the derivatives of  $u_e$ ,  $p_e$  and  $\rho_e$  from Eqs. C-3, C-5, C-6 and C-7, we obtain

$$\frac{dh_e}{dt_P} \left\{ \frac{1}{u_e^2} \frac{\rho_e}{p_e} \right\} + \frac{1}{z_e} \frac{dz_e}{dt_P} + \frac{1}{T_e} \frac{dT_e}{dt_P} - \frac{1}{A} \frac{dA}{dt_P} = 0 \quad (C-8)$$

Now for any given set of reactions and reaction rates the enthalpy derivative can be expressed in the form  $\frac{dh_e}{dt_P} = B_1 + B_2 \frac{dT_e}{dt_P}$ , where the coefficients  $B_1$  and  $B_2$  involve derivatives of species concentrations  $\frac{dX_i}{dt_P}$  and of vibrational temperature  $\frac{dT_{vi}}{dt_P}$ , and these are all functions of local gas properties only. The value of  $\frac{dz_e}{dt_P} = \sum \frac{dX_i}{dt_P}$  is also a function of local gas properties only.

Consequently, Eq. (8) provides a direct specification  $\frac{dT_e}{dt_P}$  provided  $\frac{dA}{dt_P}$  is known. Values of the derivatives of  $h_e$ ,  $u_e$ ,  $p_e$  and  $\rho_e$  then follow directly from the above equations.

The Avco Everett Research Laboratory stream-tube program was modified along the lines indicated above, with the area variation of the diverging channel specified with the aid of Mirels' work. For a laminar boundary layer and a given value of limiting separation distance  $x_l$ , the area variation experienced by the shocked gas is given by

$$A_o/A = (\rho_e u_e)/(\rho_l U_s) = 1 - (x/x_l)^n, \text{ with } n = 0.5. \quad (C-9)$$

The same expression with  $n = 0.8$  is applicable for a turbulent boundary layer provided an appropriate value of  $x_l$  is used.

Only one difficulty remains in the application of this model for interpretation of the present experiments. It may be noted that

$$\frac{1}{A} \frac{dA}{dt_P} = \frac{u_e}{A} \frac{dA}{dx} = \frac{A}{A_o} \frac{n u_e}{x_l} \left( \frac{x}{x_l} \right)^{n-1}$$

tends to a value of infinity when  $x$  approaches zero. The resulting computational problems can be circumvented by assuming that in the region  $0 < x < x_m$  the area variation is linear, with  $A/A_o = 1 + Kx$ , where



K is determined from  $\{1 + Kx_m\}^{-1} = 1 - (x_m/x_l)^n$ . In choosing an appropriate value of  $x_m$ , some recourse may be made to the physical situation in the experiment. The theoretical analysis of the boundary layer growth assumes that this growth commences immediately behind a plane shock wave of infinitesimal thickness, whereas the experiment involves a slightly curved shock wave for which the translational/rotational relaxation thickness is approximately four times the mean free path in the unshocked gas.

For the 1.5 inch diameter shock tube the translational/rotational relaxation thickness is  $\delta_s \approx 0.02/p_1$  cm, with  $p_1$  in torr. For the curvature, the effective thickness is  $\delta_c \approx 0.1/\sqrt{p_1}$  cm, again with  $p_1$  in torr. It seems physically reasonable to choose  $x_m$  of the same order of magnitude as either of these experimental quantities, and the present calculations use a geometric mean,

$$x_m = \sqrt{\delta_c \delta_s} \approx .045/p_1^{0.75} \text{ cm.}$$

Check calculations were made to ensure that the results were in no way sensitive to this choice.

Several kinetics calculations were made for comparison with the data of the present experiments, using Eqs. (C-8) and (C-9). The values of  $x_l$  used are shown as functions of shock speed in Fig. C-2. The solid curves A and B are obtained from Mirels' theory<sup>43</sup> for a shock tube of 1.5 inches diameter with a laminar boundary layer, for initial pressures of 1 torr and 5 torr respectively. At a given shock speed the theoretical value of  $x_l$  scales linearly with  $p_1$ . However, at an observation station 18 feet from the shock tube diaphragm, (as in the present experiments) the theoretical length of the "test slug" would be approximately 40% of  $x_l$  for  $p_1 = 5$  torr, and almost 100% of  $x_l$  for  $p_1 = 1$  torr. The prediction for the 1 torr case is in quite good agreement with the experimental test times, which are shown (converted into test lengths) as the curve C of Fig. C-2. The effect of using curve A or curve C of Fig. C-2 in the calculations is shown in Fig. C-3. For  $p_1 = 5$  torr, the predictions using a laminar and a turbulent boundary layer were not in good agreement with the experimental results.

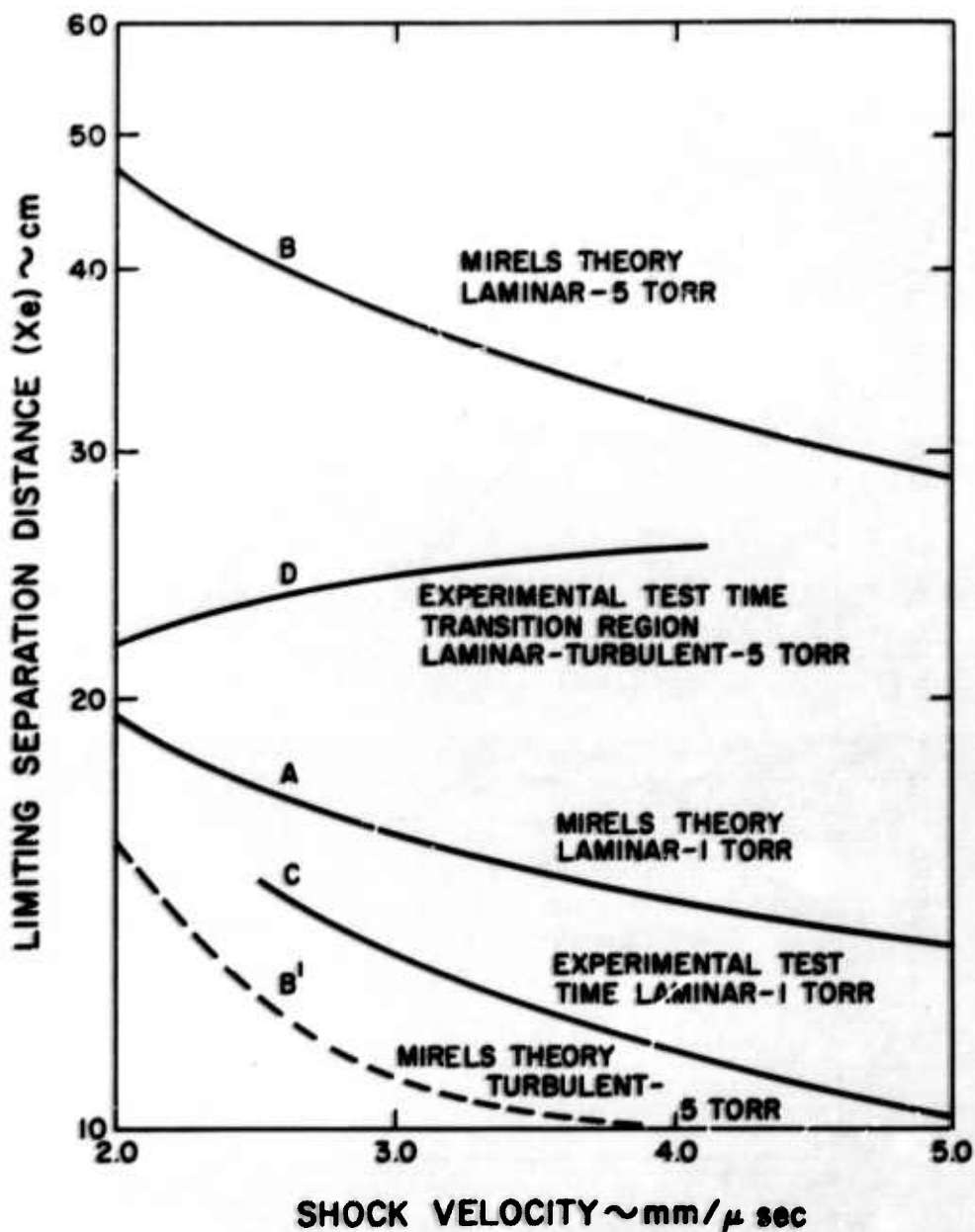


Fig. C-2 The limiting separation distance, experimental and theoretically as a function of shock.



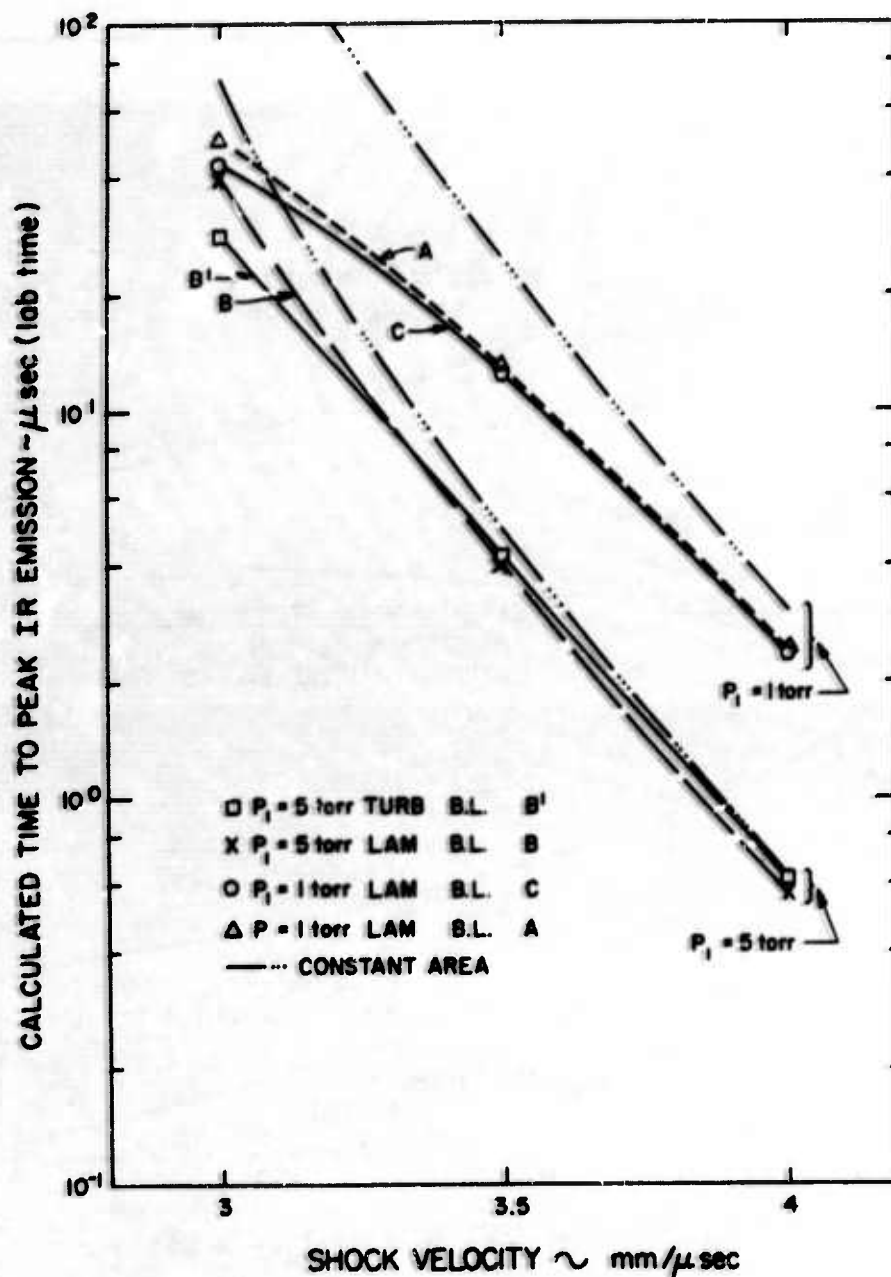


Fig. C-3 A comparison of calculating the times to peak using various limiting separation distances as a function of shock velocity. The times to peak, using no boundary layer correction, is also shown.

Side wall heat transfer gauge measurements indicated that the boundary layer might be in a transition mode. The experimental test time for  $p_1 = 5$  torr is shown as curve D on Fig. C-2. One should note that at the lower shock velocities the test time agrees more closely with the turbulent boundary layer predictions,<sup>46</sup> Fig. C-2, curve B', but at higher shock velocities the data are in better agreement with the laminar prediction,<sup>43</sup> curve B. The choice of an appropriate value of  $x_l$  for  $p_1 = 5$  torr is very difficult. Calculations were made using the laminar and turbulent predictions. The true value of  $x_l$  lies between these extremes, with the initial variation of area corresponding to a laminar boundary layer growth followed by a transition to a turbulent boundary layer at some value of  $x < x_l$ . The effect of using either the laminar or turbulent boundary layer on the calculations is shown in Fig. C-3 by the curves labeled B and B'.

All the calculations discussed below use the rate constants shown in Table I, except for modification of the catalytic efficiencies of  $O_2$  and O in dissociating  $O_2$ <sup>47</sup> and deletion of the bimolecular reaction  $N_2 + O_2 \rightarrow 2NO$ .

Figure C-3 shows the results of several calculations of time to peak infrared emission from the NO formed behind the normal shock wave in the present experiments. The calculations are for  $p_1 = 1$  torr and 5 torr. The dotted-dashed curves are for one-dimensional constant area flow, with no boundary layer correction. These two curves are separated by a factor of 5 over the entire range plotted, since binary reactions predominate (at the low speed end of the  $p_1 = 5$  torr curve the 3 body reactions are just becoming significant near the time of peak infrared emission) in determining the gas behavior, resulting in flow times which scale inversely with  $p_1$  for a given shock speed. However, when area variation is introduced into Eq. C-8, it is clear that this binary scaling will be invalidated unless  $\frac{1}{A} \frac{dA}{dt_P}$  scales inversely with  $p_1$ ; i.e., unless  $x_l \propto p_1^{-1}$ . For the calculations with area variation due to boundary layer growth shown in Figs. 20-22 (solid and dashed curves), the values of  $x_l$  used do not satisfy this scaling relationship. The solid curves obtained show a trend which is consistent with the experimental data, and give reasonable agreement with those data for times to a fraction of the peak radiation less than 15 microseconds. Unfortunately, most of the data points yielding times in excess of 15 microseconds are influenced to some extent by shock speed attenuation, so that the boundary layer growth effects alone cannot provide adequate correction over the entire shock velocity range.

## REFERENCES

1. R. R. Gilmore, Rand Corporation RM-1543, August 24, 1955.
2. N. Davidson, Avco Everett Research Laboratory, Research Report 32, June 1958.
3. M. M. Bortner and J. A. Golden, General Electric Missile and Space Vehicle Department Report No. R61SD23, February 1961.
4. K. L. Wray, Progress in Astronautics and Rocketry, edited by F. R. Riddel (Academic Press, New York, 1962) Vol. 7, p. 181.
5. H. S. Glick, J. J. Klein and W. Squire, J. Chem. Phys. 27, 850 (1957).
6. R. E. Duff and N. Davidson, J. Chem. Phys. 31, 1081 (1959).
7. M. Camac and A. Vaughan, J. Chem. Phys. 34, 460 (1961).
8. S. R. Byron, J. Chem. Phys. 30, 1380 (1959)
9. K. L. Wray and J. D. Teare, J. Chem. Phys. 36, 2582 (1962)
10. F. Kaufman and J. R. Kelso, J. Chem. Phys. 23, 1702 (1955)
11. E. Freedman and J. W. Daiber, J. Chem. Phys. 34, 1271 (1961)
12. J. J. Allport, Lockheed Aircraft Corp. LMSD-288226, January, 1960.
13. K. G. P. Sulzmann and C. B. Ludwig, Convair Division of General Dynamics Corp. ZPh-087, March 1961.
14. C. P. Fenimore and G. W. Jones, Eighth Symposium on Combustion 127, (1960).
15. G. Herzberg, "Spectra of Diatomic Molecules," D. Van Nostrand Company, Inc., New York, 1950.
16. C. E. Moore, Atomic Energy Levels, N. B. S. Circular No. 467 (1949)
17. R. J. Rubin and K. E. Shuler, J. Chem. Phys. 25, 59 (1956)

18. R. J. Havens, dissertation, University of Wisconsin, Madison, Wisconsin (1938).
19. H. L. Dinsmore, dissertation, University of Minnesota, Minneapolis, Minnesota (1949).
20. S. S. Penner and D. Weber, J. Chem. Phys. 21, 649 (1953).
21. J. Vincent-Geiss, Compt. Rend. 239, 251 (1954).
22. B. Schurin and S. A. Clough, J. Chem. Phys. 38, 1855 (1963).
23. T. C. James, J. Chem. Phys. 40, 762 (1964).
24. J. C. Breeze and C. C. Ferrisco, J. Chem. Phys. 41, 3420 (1964).
25. K. Fukuda, J. Chem. Phys. 42, 521 (1965).
26. D. Ford and J. H. Shaw, Bull. Am. Phys. Soc II, 10, 636 (1965).
27. L. L. Abels and J. H. Shaw, J. Mol. Spectr., 20, 11 (1966).
28. P. Varanasi and S. S. Penner, J. Q. S. R. T. (in press) (1966).
29. R. C. Millikan and D. R. White, J. Chem. Phys. 39, 98 (1963).
30. D. R. White and R. C. Millikan, AIAA J. 2, 1844 (1964).
31. R. Taylor, M. Camac and R. M. Feinberg, Avco Everett Research Laboratory Research Report 250, May 1966 and Proceedings of Eleventh Symposium (International) on Combustion (1966).
32. K. L. Wray, J. Chem. Phys. 37, 1254 (1962).
33. K. L. Wray, Tenth Symposium (International) on Combustion 523, (1965).
34. M. Camac, J. Chem. Phys. 34, 448 (1961).
35. R. C. Millikan and D. R. White, J. Chem. Phys. 39, 1803 (1963).
36. V. H. Blackman, J. Fluid Mech. 1, 61 (1956).

37. K. L. Wray, J. Chem. Phys. 36, 2597 (1962).
38. F. Robben, J. Chem. Phys. 31, 420 (1959).
39. R. N. Schwartz, Z. I. Slawsky and K. F. Herzfeld, J. Chem. Phys. 20, 1591 (1952).
40. R. G. Breen, Jr., J. Chem. Phys. 25, 512 (1958).
41. R. O'B. Carpenter and M. A. Franzosa, J. Quant. Spectroscopy and Radiat. Transfer., 5, 465 (1965).
42. S. S. Penner, "Quantitative Molecular Spectroscopy and Gas Emissivities," Addison-Wesley Publishing Co., Inc. Reading, Mass. (1959).
43. H. Mirels, Phys. Fluids 6, 1201 (1963).
44. R. E. Duff, Phys. Fluids 2, 207 (1959).
45. S. C. Lin, and J. D. Teare, Proc. of 6th Symposium on Ballistic Missile and Aerospace Technology, 4, 35, New York (1961).
46. H. Mirels, AIAA J. 2, 84 (1964).
47. S. C. Lin and J. D. Teare, Phys. Fluids 6, 355 (1963).



## DOCUMENT CONTROL DATA - R&amp;D

(Security classification of title, body of abstract and indexing annotation must be entered when the overall report is classified)

1 ORIGINATING ACTIVITY (Corporate author) Avco Everett Research Laboratory 2385 Revere Beach Parkway Everett, Massachusetts		2a REPORT SECURITY CLASSIFICATION Unclassified	
		2b GROUP	
3 REPORT TITLE THE PRODUCTION OF NITRIC OXIDE IN SHOCK-HEATED AIR			
4 DESCRIPTIVE NOTES (Type of report and inclusive dates) Research Report 245			
5 AUTHOR(S) (Last name, first name, initial) Camac, Morton, Feinberg, Robert M., and Teare, J. Derek			
6 REPORT DATE December 1966		7a TOTAL NO OF PAGES 78	7b NO. OF REFS 47
8a CONTRACT OR GRANT NO. AF 04(694)-690		9a ORIGINATOR'S REPORT NUMBER(S) Research Report 245	
b PROJECT NO.		9b OTHER REPORT NO(S) (Any other numbers that may be assigned this report) BSD-TR-	
c			
d			
10 AVAILABILITY/LIMITATION NOTICES This document is subject to special export controls and each transmittal to foreign governments or foreign nationals may be made only with prior approval of: Ballistic Systems Division (BSYDV) Norton AFB, Calif. 92409.			
11 SUPPLEMENTARY NOTES		12 SPONSORING MILITARY ACTIVITY BSD - Deputy for Ballistic Missile Re-entry Systems AFSC, Norton AFB, California	
13 ABSTRACT <p>The rate of production of nitric oxide in shock-heated air was measured over the temperature range from 2300°K to 4500°K. The NO concentration was determined from the NO infrared emission in the 5.3 micron fundamental vibration-rotation band. The main production of nitric oxide was found to be by the dissociation reaction <math>O_2 + M \xrightarrow{k_4} 2O + M</math>, followed by the atomic shuttle reactions <math>O + N_2 \xrightarrow{k_2} NO + N</math> and <math>N + O_2 \xrightarrow{k_2} NO + O</math>.</p> <p>The overall rate constant <math>k = k_2 \cdot k_4</math> for NO production was found to be <math>0.40 \pm 0.12</math> of the rate constant compiled by Wray.</p> <p>The rate constant for the bimolecular reaction <math>N_2 + O_2 \rightarrow 2NO</math> was found to be less than one-tenth the value suggested by Freedman and Daiber. In order to explain the disagreement in the rate constant, experiments were performed in shock-heated nitric oxide where the depletion of nitric oxide and the reaction products were observed. It was found that the NO depletion occurs mainly via the reaction <math>2NO \rightarrow N_2 + O_2</math>.</p> <p>An analysis of the vibrational relaxation of NO-O<sub>2</sub>-N<sub>2</sub> mixtures is presented and it is shown that NO vibration lag is small and does not affect the data analysis. We determined that the integrated band intensity of the NO fundamental is <math>124 \pm 22 \text{ atm}^{-1} \text{ cm}^{-2}</math> at S. T. P.</p> <p>It is also shown that corrections due to the shock tube boundary layer must be included in order to obtain detailed agreement between experiment and calculations. The procedure for correcting chemical measurements for shock tube boundary layer growth is outlined.</p>			

(U)



- LINK A**

LINK B

LINK C

## ROLE

WT

## ROLE

51

**Hot**

11

**Security Classification**

UNCLASSIFIED

Security Classification

## DOCUMENT CONTROL DATA - R&amp;D

(Security classification of title, body of abstract and indexing annotation must be entered when the overall report is classified)

1 ORIGINATING ACTIVITY (Corporate author) Avco Everett Research Laboratory 2385 Revere Beach Parkway Everett, Massachusetts		2a REPORT SECURITY CLASSIFICATION Unclassified	
		2b GROUP	
3 REPORT TITLE THE PRODUCTION OF NITRIC OXIDE IN SHOCK-HEATED AIR			
4 DESCRIPTIVE NOTES (Type of report and inclusive dates) Research Report 245			
5 AUTHOR(S) (Last name, first name, initial) Camac, Morton, Feinberg, Robert M., and Teare, J. Derek			
6 REPORT DATE December 1966		7a TOTAL NO OF PAGES 78	7b NO. OF REFS 47
8a CONTRACT OR GRANT NO. DA-01-021-AMC-12005 (Z) b (part of Project DEFENDER) c d		9a ORIGINATOR'S REPORT NUMBER(S) Research Report 245 9b OTHER REPORT NO(S) (Any other numbers that may be assigned this report)	
10 AVAILABILITY/LIMITATION NOTICES Qualified requesters may obtain copies of this report from DDC.			
11. SUPPLEMENTARY NOTES		12. SPONSORING MILITARY ACTIVITY ARPA, monitored by the Army Missile Command, United States Army Redstone Arsenal, Alabama	
13 ABSTRACT The rate of production of nitric oxide in shock-heated air was measured over the temperature range from 2300°K to 4500°K. The NO concentration was determined from the NO infrared emission in the 5.3 micron fundamental vibration-rotation band. The main production of nitric oxide was found to be by the dissociation reaction $O_2 + M \xrightarrow{k_4} 2O + M$ , followed by the atomic shuttle reactions $O + N_2 \xrightarrow{k_2} NO + N$ and $N + O_2 \rightarrow NO + O$ . The overall rate constant $k = k_2 \cdot k_4$ for NO production was found to be $0.40 \pm 0.12$ of the rate constant compiled by Wray. The rate constant for the bimolecular reaction $N_2 + O_2 \rightarrow 2NO$ was found to be less than one-tenth the value suggested by Freedman and Daiber. In order to explain the disagreement in the rate constant, experiments were performed in shock-heated nitric oxide where the depletion of nitric oxide and the reaction products were observed. It was found that the NO depletion occurs mainly via the reaction $2NO \rightarrow N_2O + O$ . An analysis of the vibrational relaxation of NO-O <sub>2</sub> -N <sub>2</sub> mixtures is presented and it is shown that NO vibration lag is small and does not affect the data analysis. We determined that the integrated band intensity of the NO fundamental is $124 \pm 22 \text{ atm}^{-1} \text{ cm}^{-2}$ at S. T. P. It is also shown that corrections due to the shock tube boundary layer must be included in order to obtain detailed agreement between experiment and calculations. The procedure for correcting chemical measurements for shock tube boundary layer growth is outlined.  (U)			

[illegible]

## INSTRUCTIONS

- 1. ORIGINATING ACTIVITY:** Enter the name and address of the contractor, subcontractor, grantee, Department of Defense activity or other organization (corporate author) issuing the report.

- 2a. **REPORT SECURITY CLASSIFICATION:** Enter the overall security classification of the report. Indicate whether "Restricted Data" is included. Marking is to be in accordance with appropriate security regulations.

- 2b. GROUP: Automatic downgrading is specified in DoD Directive 5200.10 and Armed Forces Industrial Manual. Enter the group number. Also, when applicable, show that optional markings have been used for Group 3 and Group 4 as authorized.

3. **REPORT TITLE:** Enter the complete report title in all capital letters. Titles in all cases should be unclassified. If a meaningful title cannot be selected without classification, show title classification in all capitals in parentheses immediately following the title.

4. **DESCRIPTIVE NOTES:** If appropriate, enter the type of report, e.g., interim, progress, summary, annual, or final. Indicate the inclusive dates when a specific reporting period is covered.

5. **AUTHORS:** Enter the name(s) of author(s) as shown on or in the report. Enter last name, first name, middle initial. If military, show rank and branch of service. The name of the principal author is an absolute minimum requirement.

6. **REPORT DATE:** Enter the date of the report as day, month, year, or month, year. If more than one date appears on the report, use date of publication.

- 7a. **TOTAL NUMBER OF PAGES:** The total page count should follow normal pagination procedures, i.e., enter the number of pages containing information.

- 7b. NUMBER OF REFERENCES Enter the total number of references cited in the report.

- 8.a. **CONTRACT OR GRANT NUMBER:** If appropriate, enter the applicable number of the contract or grant under which the report was written.

- 8b, 8c, & 8d. PROJECT NUMBER: Enter the appropriate military department identification, such as project number, subproject number, system numbers, task number, etc.

- 9a. **ORIGINATOR'S REPORT NUMBER(S):** Enter the official report number by which the document will be identified and controlled by the originating activity. This number must be unique to this report.

- 9b. OTHER REPORT NUMBER(S): If the report has been assigned any other report numbers (either by the originator or by the sponsor), also enter this number(s).

10. AVAILABILITY/LIMITATION NOTICES: Enter any limitations on further dissemination of the report, other than those

Imposed by security classification, using standard statements such as:

- (1) "Qualified requesters may obtain copies of this report from DDC."
- (2) "Foreign announcement and dissemination of this report by DDC is not authorized."
- (3) "U. S. Government agencies may obtain copies of this report directly from DDC. Other qualified DDC users shall request through \_\_\_\_\_."
- (4) "U. S. military agencies may obtain copies of this report directly from DDC. Other qualified users shall request through \_\_\_\_\_."
- (5) "All distribution of this report is controlled. Qualified DDC users shall request through \_\_\_\_\_."

If the report has been furnished to the Office of Technical Services, Department of Commerce, for sale to the public, indicate this fact and enter the price, if known.

11. **SUPPLEMENTARY NOTES:** Use for additional explanatory notes.

12. **SPONSORING MILITARY ACTIVITY:** Enter the name of the departmental project office or laboratory sponsoring (paying for) the research and development. Include address.

13. **ABSTRACT:** Enter an abstract giving a brief and factual summary of the document indicative of the report, even though it may also appear elsewhere in the body of the technical report. If additional space is required, a continuation sheet shall be attached.

It is highly desirable that the abstract of classified reports be unclassified. Each paragraph of the abstract shall end with an indication of the military security classification of the information in the paragraph, represented as (TS), (S), (C) or (U)

There is no limitation on the length of the abstract. However, the suggested length is from 150 to 225 words.

14. **KEY WORDS:** Key words are technically meaningful terms or short phrases that characterize a report and may be used as index entries for cataloging the report. Key words must be selected so that no security classification is required. Identifiers, such as equipment model designation, trade name, military project code name, geographic location, may be used as key words but will be followed by an indication of technical context. The assignment of links, rules, and weights is optional.